

HIGHER-ORDER DGFEM TRANSPORT CALCULATIONS ON POLYTOPE  
MESHES FOR MASSIVELY-PARALLEL ARCHITECTURES

A Dissertation

by

MICHAEL WAYNE HACKEMACK

Submitted to the Office of Graduate and Professional Studies of  
Texas A&M University  
in partial fulfillment of the requirements for the degree of

DOCTOR OF PHILOSOPHY

Chair of Committee,	Jean Ragusa
Committee Members,	Marvin Adams
	Jim Morel
	Nancy Amato
	Troy Becker
Head of Department,	Yassin Hassan

May 2016

Major Subject: Nuclear Engineering

Copyright 2016 Michael Wayne Hackemack

## ABSTRACT

blah...

## DEDICATION

For the Greater Glory of God (AMDG).

“Good ideas are not adopted automatically. They must be driven into practice with courageous impatience. Once implemented, they can be easily overturned or subverted through apath or lack of follow-up - so a continuous effort is required.”

- Admiral Hyman G. Rickover

## ACKNOWLEDGEMENTS

I would like to thank my graduate advisor and committee chair, Dr. Jean Ragusa for all of his guidance towards the completion of this research endeavour. I would also like to thank my other committee members: Dr. Marvin Adams, Dr. Jim Morel, Dr. Nancy Amato, and Dr. Troy Becker for all of their support.

This research was performed under appointment to the Rickover Graduate Fellowship Program in Nuclear Engineering sponsored by the Naval Reactors Division of the United States Department of Energy.

## NOMENCLATURE

B/CS	Bryan/College Station
HSUS	Humane Society of the United States
P	Pressure
T	Time
TVA	Tennessee Valley Authority
TxDOT	Texas Department of Transportation

# TABLE OF CONTENTS

	Page
ABSTRACT . . . . .	ii
DEDICATION . . . . .	iii
ACKNOWLEDGEMENTS . . . . .	iv
NOMENCLATURE . . . . .	v
TABLE OF CONTENTS . . . . .	vi
LIST OF FIGURES . . . . .	viii
LIST OF TABLES . . . . .	x
1. INTRODUCTION . . . . .	1
1.1 Current State of the Problem . . . . .	1
1.2 Purpose of the Dissertation . . . . .	1
1.3 Organization of the Dissertation . . . . .	1
2. THE DGFEM FORMULATION OF THE MULTIGROUP $S_N$ EQUATIONS . . . . .	2
2.1 The Neutron Transport Equation . . . . .	3
2.2 Energy Discretization . . . . .	5
2.3 Angular Discretization . . . . .	9
2.3.1 Level-Symmetric Quadrature Set . . . . .	10
2.3.2 Product Gauss-Legendre-Chebyshev Quadrature Set . . . . .	10
2.4 Spatial Discretization . . . . .	13
2.4.1 Elementary Mass Matrices . . . . .	19
2.4.2 Elementary Streaming Matrices . . . . .	21
2.4.3 Elementary Surface Matrices . . . . .	22
2.5 Solution Procedures . . . . .	22
2.5.1 Angle and Energy Iteration Procedures . . . . .	24
2.5.1.1 Source Iteration . . . . .	24
2.5.1.2 Krylov Subspace Methods - GMRES . . . . .	24
2.5.2 Spatial Solution Procedures . . . . .	24
2.5.2.1 Transport Sweeping . . . . .	24

2.5.2.2	Adaptive Mesh Refinement Procedures . . . . .	24
2.6	Conclusions . . . . .	24
3.	FEM BASIS FUNCTIONS FOR UNSTRUCTURED POLYTOPES . . . . .	26
3.1	Linear Basis Functions on 2D Polygons . . . . .	26
3.1.1	Traditional Linear Basis Functions - $\mathbb{P}_1$ and $\mathbb{Q}_1$ Spaces . . . . .	27
3.1.2	Wachspress Rational Basis Functions . . . . .	28
3.1.3	Piecewise Linear (PWL) Basis Functions . . . . .	28
3.1.4	Mean Value Basis Functions . . . . .	29
3.1.5	Maximum Entropy Basis Functions . . . . .	29
3.1.6	Summary of 2D Linear Basis Functions on Polygons . . . . .	29
3.2	Quadratic Serendipity Basis Functions on 2D Polygons . . . . .	29
3.2.1	Traditional Quadratic Basis Functions - $\mathbb{P}_2$ and $\mathbb{S}_2$ Spaces . . . . .	29
3.2.2	Quadratic Mean Value Coordinates on 2D Polygons . . . . .	29
3.2.3	Quadratic Maximum Entropy Coordinates on 2D Polygons . . . . .	29
3.3	Linear Basis Functions on 3D Polyhedra . . . . .	29
3.3.1	3D Linear and TriLinear Basis Functions . . . . .	29
3.3.2	3D Piecewise Linear (PWL) Basis Functions . . . . .	30
3.4	Numerical Results . . . . .	33
3.4.1	Two-Dimensional Exactly-Linear Transport Solutions . . . . .	34
3.4.2	Convergence Rate Analysis by the Method of Manufactured Solutions . . . . .	36
3.4.3	Searchlight Problem . . . . .	44
3.5	Conclusions . . . . .	45
	REFERENCES . . . . .	47

# LIST OF FIGURES

FIGURE	Page
2.1 Interval structure of the multigroup methodology. . . . .	6
2.2 Level-Symmetric angular quadrature set . . . . .	11
2.3 Product Gauss-Legendre-Chebyshev angular quadrature set . . . . .	14
2.4 Two cells of the spatial discretization . . . . .	16
2.5 Scattering matrices with and without upscattering . . . . .	23
2.6 blah . . . . .	24
2.7 blah . . . . .	25
3.1 Arbitrary polygon with geometric properties used for 2D basis function generation. . . . .	26
3.2 Contour plots of the PWL basis functions on the unit square for the vertices located at: (a) (0,0), (b) (1,0), (c) (1,1), and (d) (0,1). . . . .	29
3.3 Vertex structure for a (a) regular pentagonal cell and a (b) degenerate pentagonal cell. . . . .	30
3.4 Contour plots of the PWL basis functions for a regular pentagon: (a) and (c) as well as a degenerate pentagon: (b) and (d). . . . .	31
3.5 Plots of the PWL basis functions for a regular pentagon: (a) and (c) as well as a degenerate pentagon: (b) and (d). . . . .	32
3.6 Vertex structure for the (a) unit square and (b) unit cube. . . . .	32
3.7 Contour plots of the exactly-linear solution with the Wachspress basis functions on (a) cartesian mesh, (b) ordered-triangular mesh, (c) quadrilateral shestakov mesh, (d) sinusoidal polygonal mesh, (e) quadrilateral z-mesh, and (f) polygonal z-mesh. . . . .	37



3.8	Contour plots of the exactly-linear solution with the PWL basis functions on (a) cartesian mesh, (b) ordered-triangular mesh, (c) quadrilateral shestakov mesh, (d) sinusoidal polygonal mesh, (e) quadrilateral z-mesh, and (f) polygonal z-mesh. . . . .	38
3.9	Contour plots of the exactly-linear solution with the mean value basis functions on (a) cartesian mesh, (b) ordered-triangular mesh, (c) quadrilateral shestakov mesh, (d) sinusoidal polygonal mesh, (e) quadrilateral z-mesh, and (f) polygonal z-mesh. . . . .	39
3.10	Contour plots of the exactly-linear solution with the linear maximum entropy basis functions on (a) cartesian mesh, (b) ordered-triangular mesh, (c) quadrilateral shestakov mesh, (d) sinusoidal polygonal mesh, (e) quadrilateral z-mesh, and (f) polygonal z-mesh. . . . .	40
3.11	Contour plots of the exactly-linear solution with the quadratic serendipity maximum entropy basis functions on (a) cartesian mesh, (b) ordered-triangular mesh, (c) quadrilateral shestakov mesh, (d) sinusoidal polygonal mesh, (e) quadrilateral z-mesh, and (f) polygonal z-mesh. . . . .	41
3.12	Initial mesh configuration for the searchlight problem before any refinement cycles. . . . .	45
3.13	Exiting angular flux on the right boundary with uniform refinement using the (a) Wachspress basis functions, (b) PWL basis functions, (c) mean value basis functions, (d) linear maximum entropy coordinates and (e) quadratic serendipity maximum entropy coordinates. . . . .	46

## LIST OF TABLES

TABLE		Page
2.1	2D angle mapping from the first quadrant into the other 3 quadrants.	10
2.2	3D angle mapping from the first octant into the other 7 octants. . . .	10

## 1. INTRODUCTION

### 1.1 Current State of the Problem

### 1.2 Purpose of the Dissertation

### 1.3 Organization of the Dissertation

In this introductory chapter, we have presented a summary of work performed. We also gave our motivation for choosing this work as well as a brief discussion of previous work that has directly influenced this dissertation. We conclude this introduction by briefly describing the remaining chapters of this dissertation.

## 2. THE DGFEM FORMULATION OF THE MULTIGROUP $S_N$ EQUATIONS

The movement of bulk materials and particles through some medium can be described with the statistical behavior of a non-equilibrium system. Boltzmann first devised these probabilistic field equations to characterize fluid flow via driving temperature gradients [1]. His work was later extended to model general fluid flow, heat conduction, hamiltonian mechanics, quantum theory, general relativity, and radiation transport, among others. The Boltzmann Equation can be written in the general form:

$$\frac{\partial u}{\partial t} = \left( \frac{\partial u}{\partial t} \right)_{force} + \left( \frac{\partial u}{\partial t} \right)_{advec} + \left( \frac{\partial u}{\partial t} \right)_{coll} \quad (2.1)$$

where  $u(\vec{r}, \vec{p}, t)$  is the transport distribution function parameterized in terms of position,  $\vec{r} = (x, y, z)$ , momentum,  $\vec{p} = (p_x, p_y, p_z)$ , and time,  $t$ . In simplified terms, Eq. (2.1) can be interpreted that the time rate of the change of the distribution function,  $\frac{\partial u}{\partial t}$ , is equal to the sum of the change rates due to external forces,  $\left( \frac{\partial u}{\partial t} \right)_{force}$ , advection of the particles,  $\left( \frac{\partial u}{\partial t} \right)_{advec}$ , and particle-to-particle and particle-to-matter collisions,  $\left( \frac{\partial u}{\partial t} \right)_{coll}$  [2].

For neutral particle transport, the following assumptions [3] about the behavior of the radiation particles can be utilized:

1. Particles may be considered as points;
2. Particles do not interact with other particles;
3. Particles interact with material target atoms in a binary manner;
4. Collisions between particles and material target atoms are instantaneous;

5. Particles do not experience any external force fields (*e.g.* gravity).

These assumptions lead to the first order form of the Boltzmann Transport Equation, which we simply call the transport equation for brevity. The remainder of the chapter is layed out as follows. Section 2.1 provides the general form of the neutron transport equation with some variants. Section 2.2 describes how we discretize the transport equation in energy with the multigroup methodology and Section 2.3 presents the angular discretization via collocation. Section 2.4 will conclude our discretization procedures in the spatial domain. Section 2.5 will present the iterative procedures used to converge our solution space. We then present concluding remarks for the chapter in Section 2.6.

## 2.1 The Neutron Transport Equation

The time-dependent neutron angular flux,  $\Psi(\vec{r}, E, \vec{\Omega}, t)$ , at spatial position  $\vec{r}$ , with energy  $E$  moving in direction  $\vec{\Omega}$  and at time  $t$ , is defined within an open, convex spatial domain  $\mathcal{D}$ , with boundary,  $\partial\mathcal{D}$  by the general neutron transport equation:

$$\begin{aligned} \frac{\partial \Psi}{\partial t} + \vec{\Omega} \cdot \vec{\nabla} \Psi(\vec{r}, E, \vec{\Omega}, t) + \sigma_t(\vec{r}, E, t) \Psi(\vec{r}, E, \vec{\Omega}, t) &= Q_{ext}(\vec{r}, E, \vec{\Omega}, t) \\ &+ \frac{\chi(\vec{r}, E, t)}{4\pi} \int dE' \nu \sigma_f(\vec{r}, E', t) \int d\Omega' \Psi(\vec{r}, E', \vec{\Omega}', t) \\ &+ \int dE' \int d\Omega' \sigma_s(E' \rightarrow E, \Omega' \rightarrow \Omega) \Psi(\vec{r}, E', \vec{\Omega}') \end{aligned} \quad (2.2)$$

with the following, general boundary condition:

$$\begin{aligned} \Psi(\vec{r}, E, \vec{\Omega}, t) &= \Psi^{inc}(\vec{r}, E, \vec{\Omega}, t) + \int dE' \int d\Omega' \gamma(\vec{r}, E' \rightarrow E, \vec{\Omega}' \rightarrow \vec{\Omega}, t) \Psi(\vec{r}, E', \vec{\Omega}', t) \\ &\quad \text{for } \vec{r} \in \partial\mathcal{D}^- \left\{ \partial\mathcal{D}, \vec{\Omega}' \cdot \vec{n} < 0 \right\}. \end{aligned} \quad (2.3)$$

In Eqs. (2.2) and (2.3), the physical properties of the system are defined as the following:  $\sigma_t(\vec{r}, E, t)$  is the total neutron cross section,  $\chi(\vec{r}, E, t)$  is the neutron fission spectrum,  $\sigma_f(\vec{r}, E', t)$  is the fission cross section,  $\nu(\vec{r}, E', t)$  is the average number of neutrons emitted per fission,  $\sigma_s(E' \rightarrow E, \Omega' \rightarrow \Omega, t)$  is the scattering cross section, and  $Q_{ext}(\vec{r}, E, \vec{\Omega}, t)$  is a distributed external source.

We can simplify Eq. (2.2) to:

$$\frac{\partial \Psi}{\partial t} + \mathbf{L}\Psi = \mathbf{F}\Psi + \mathbf{S}\Psi + \mathbf{Q}, \quad (2.4)$$

by dropping the dependent variable parameters and using the following operators:

$$\begin{aligned} \mathbf{L}\Psi &= \vec{\Omega} \cdot \vec{\nabla} \Psi(\vec{r}, E, \vec{\Omega}, t) + \sigma_t(\vec{r}, E, t) \Psi(\vec{r}, E, \vec{\Omega}, t), \\ \mathbf{F}\Psi &= \frac{\chi(\vec{r}, E, t)}{4\pi} \int dE' \nu \sigma_f(\vec{r}, E', t) \int d\Omega' \Psi(\vec{r}, E', \vec{\Omega}', t), \\ \mathbf{S}\Psi &= \int dE' \int d\Omega' \sigma_s(E' \rightarrow E, \Omega' \rightarrow \Omega, t) \Psi(\vec{r}, E', \vec{\Omega}', t), \\ \mathbf{Q} &= Q_{ext}(\vec{r}, E, \vec{\Omega}, t), \end{aligned} \quad (2.5)$$

where  $\mathbf{L}$  is the loss operator which includes total reaction and streaming,  $\mathbf{F}$  is the fission operator, and  $\mathbf{S}$  is the scattering operator. If we wish to analyze a transport problem at steady-state conditions, we simply drop the temporal derivative to form

$$\mathbf{L}\Psi = \mathbf{F}\Psi + \mathbf{S}\Psi + \mathbf{Q}, \quad (2.6)$$

and note that the operators of Eq. (2.5) no longer depend on time,  $t$ .

There is a special subset of transport problems that is routinely analyzed to determine the neutron behavior of a fissile system called the *k-eigenvalue problem*. In Eq. (2.2),  $\nu(\vec{r}, E)$  acts as a multiplicative factor on the number of neutrons emitted per fission event. We replace this multiplicative factor in the following manner:

$$\nu(\vec{r}, E) \rightarrow \frac{\tilde{\nu}(\vec{r}, E)}{k}, \quad (2.7)$$

where we have introduced the eigenvalue,  $k$ . By also dropping the external source term, the steady-state neutron transport equation in Eq. (2.6) can be rewritten into

$$(\mathbf{L} - \mathbf{S}) \tilde{\Psi} = \frac{1}{k} \mathbf{F} \tilde{\Psi}, \quad (2.8)$$

where  $(k, \tilde{\Psi})$  forms an appropriate eigenvalue-eigenvector pair. Of most interest is the eigenpair corresponding to the eigenvalue of largest magnitude.

We can then gain knowledge of the behavior of the neutron population in the problem by taking the full phase-space integrals of the loss operator  $\int \int \int \mathbf{L} \tilde{\Psi} dE d\Omega d\vec{r}$ , the fission operator  $\int \int \int \mathbf{F} \tilde{\Psi} dE d\Omega d\vec{r}$ , and the scattering operator  $\int \int \int \mathbf{S} \tilde{\Psi} dE d\Omega d\vec{r}$ . With the appropriate eigenvector solution,  $\tilde{\Psi}$ , the  $k$  eigenvalue then has the meaning as the multiplicative value which balances Eq. (2.8) in an integral sense. This means that  $k$  also has a physical meaning as well. A value  $k < 1$  is called subcritical and corresponds to a system whose neutron population decreases in time; a value  $k = 1$  is called critical and corresponds to a system whose neutron population remains constant in time; and a value  $k > 1$  is called supercritical and corresponds to a system whose neutron population increases in time [4].

## 2.2 Energy Discretization

We begin our discretization procedures by focusing on the angular flux's energy variable. An ubiquitous energy discretization procedure in the transport community is the multigroup method [5, 6]. The multigroup method is defined by splitting the angular flux solution into  $G$  number of distinct, contiguous, and non-overlapping energy intervals called groups. We begin by restricting the full energy domain,  $[0, \infty)$ ,

into a finite domain,  $E \in [E_G, E_0]$ .  $E_0$  corresponds to some maximum energy value and  $E_G$  corresponds to some minimum energy value (typically 0). We have done this by defining  $G + 1$  discrete energy values that are in a monotonically continuous reverse order:  $E_G < E_{G-1} < \dots < E_1 < E_0$ .

From this distribution of energy values, we then say that a particular energy group,  $g$ , corresponds to the following energy interval:

$$\Delta E_g \in [E_g, E_{g-1}]. \quad (2.9)$$

Figure 2.1 provides a visual representation between the  $G + 1$  discrete energy values and the  $G$  energy groups. While the order that we have prescribed may seem illogical (high-to-low) to those outside of the radiation physics community, it has been historically applied this way because radiation transport problems are iteratively solved from high energy to low energy. If the group structure is well chosen, then the transport solution can be more efficiently and easily obtained with this high-to-low energy group structure.

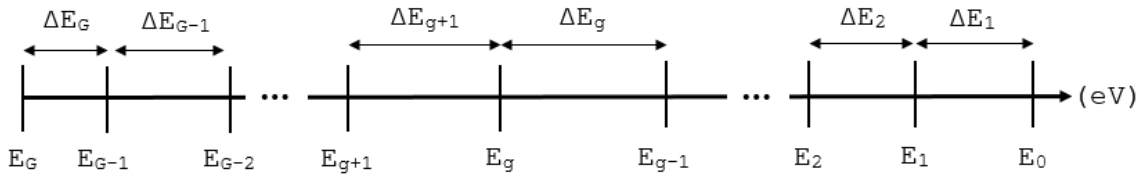


Figure 2.1: Interval structure of the multigroup methodology.

For the remainder of this energy discretization procedure, we will utilize the steady-state form of the transport equation in Eq. (2.6). The time-dependent and eigenvalue forms are analogous and would be derived identically. Taking the energy



interval for group  $g$  as defined in Eq. (2.9), the energy-integrated angular flux of group  $g$  is

$$\Psi_g(\vec{r}, \vec{\Omega}) = \int_{E_g}^{E_{g-1}} \Psi(\vec{r}, E, \vec{\Omega}) dE. \quad (2.10)$$

We can then use the energy-integrated angular flux to form the following coupled, ( $g = 1, \dots, G$ ), discrete equations (we have dropped the spatial parameter and some of the angular parameters for further clarity):

$$\left( \vec{\Omega} \cdot \vec{\nabla} + \sigma_{t,g} \right) \Psi_g = \sum_{g'=1}^G \left[ \frac{\chi_g}{4\pi} \nu \sigma_{f,g'} \int_{4\pi} \Psi_{g'}(\vec{\Omega}') d\Omega' + \int_{4\pi} \sigma_s^{g' \rightarrow g}(\vec{\Omega}', \vec{\Omega}) \Psi_{g'}(\vec{\Omega}') d\Omega' \right] + Q_g \quad (2.11)$$

where

$$\begin{aligned} \sigma_{t,g}(\vec{r}, \vec{\Omega}) &\equiv \frac{\int_{E_g}^{E_{g-1}} \sigma_t(\vec{r}, \vec{\Omega}, E) \Psi(\vec{r}, \vec{\Omega}, E) dE}{\int_{E_g}^{E_{g-1}} \int_{4\pi} \Psi(\vec{r}, \vec{\Omega}, E) dE} \\ \nu \sigma_{f,g}(\vec{r}) &\equiv \frac{\int_{E_g}^{E_{g-1}} \nu \sigma_f(\vec{r}, E) \int_{4\pi} \Psi(\vec{r}, \vec{\Omega}, E) dE d\Omega}{\int_{E_g}^{E_{g-1}} \int_{4\pi} \Psi(\vec{r}, \vec{\Omega}, E) dE d\Omega} \\ \chi_g &\equiv \int_{E_g}^{E_{g-1}} \chi(\vec{r}, E) dE \\ \sigma_s^{g' \rightarrow g}(\vec{r}, \vec{\Omega}', \vec{\Omega}) &\equiv \frac{\int_{E_{g'}}^{E_{g'-1}} \left[ \int_{E_g}^{E_{g-1}} \sigma_s(\vec{r}, E' \rightarrow E, \vec{\Omega}', \vec{\Omega}) dE \right] \Psi(\vec{r}, \vec{\Omega}', E') dE'}{\int_{E_g}^{E_{g-1}} \Psi(\vec{r}, \vec{\Omega}, E) dE} \\ Q_g(\vec{r}, \vec{\Omega}) &\equiv \int_{E_g}^{E_{g-1}} Q(\vec{r}, \vec{\Omega}, E) dE \end{aligned} \quad (2.12)$$

The above equations are mathematically exact to those presented in Eqs. (2.2 - 2.6) and we have made no approximations at this time. However, this requires full knowledge of the energy distribution of the angular flux solution at all positions in

our problem domain since we weight the multigroup cross sections with this solution. This is obviously impossible since the energy distribution is part of the solution space we are trying to solve for. Instead, we now define the process to make the multigroup discretization an effective approximation method.

We first define an approximate angular flux distribution for a region  $s$ :

$$\Psi(\vec{r}, \vec{\Omega}, E) = \hat{\Psi}(\vec{r}, \vec{\Omega}) f_s(E), \quad (2.13)$$

which is a factorization of the angular flux solution into a region-dependent energy function,  $f_s(E)$ , and a spatially/angularly dependent function,  $\hat{\Psi}(\vec{r}, \vec{\Omega})$ . With this approximation, we can redefine the energy-collapsed cross sections of Eq. (2.12):

$$\begin{aligned} \sigma_{t,g}(\vec{r}, \vec{\Omega}) &\equiv \frac{\int_{E_g}^{E_{g-1}} \sigma_t(\vec{r}, \vec{\Omega}, E) f_s(E) dE}{\int_{E_g}^{E_{g-1}} f_s(E) dE}, \\ \nu \sigma_{f,g}(\vec{r}) &\equiv \frac{\int_{E_g}^{E_{g-1}} \nu \sigma_f(\vec{r}, E) f_s(E) dE}{\int_{E_g}^{E_{g-1}} f_s(E) dE}, \\ \sigma_s^{g' \rightarrow g}(\vec{r}, \vec{\Omega}', \vec{\Omega}) &\equiv \frac{\int_{E_{g'}}^{E_{g'-1}} \left[ \int_{E_g}^{E_{g-1}} \sigma_s(\vec{r}, E' \rightarrow E, \vec{\Omega}', \vec{\Omega}) dE \right] f_s(E') dE'}{\int_{E_g}^{E_{g-1}} f_s(E) dE}. \end{aligned} \quad (2.14)$$

It is noted that we do not need to redefine the fission spectrum or the distributed external sources since they are not weighted with the angular flux solution. With this energy factorization, we would expect, in general, that the approximation error will tend to zero as the number of discrete energy groups increases (thereby making the energy bins thinner). This is especially true if the group structure is chosen with many more bins in energy regions with large variations in the energy solution. For certain problems, the region-dependent energy function is well understood (*i.e.* almost exactly known). This means, that for these problems, we can

achieve reasonable solution accuracy with only a few groups where the energy bins of the multigroup discretization are well chosen. A good example of these kinds of problems are thermal-spectrum nuclear reactors which have historically achieved reasonable solutions with as few as 4-10 energy groups.

### 2.3 Angular Discretization

Now that we have provided the discretization of the energy variable, we next focus on the discretization of the transport problem in angle. We will do this in two stages: 1) expand the angular flux in the scattering source and the distributed external source in spherical harmonics and 2) collocate the angular flux at the interpolation points of the trial space. We will perform these discretization procedures by taking the steady-state equation presented in Eq. (2.6), dropping the fission term and spatial parameterization, and using only 1 energy group:

$$\vec{\Omega} \cdot \vec{\nabla} \Psi(\vec{\Omega}) + \sigma_t \Psi(\vec{\Omega}) = \int_{4\pi} d\Omega' \sigma_s(\vec{\Omega}' \cdot \vec{\Omega}) \Psi(\vec{\Omega}') + Q(\vec{\Omega}). \quad (2.15)$$

We first expand the angular flux and the scattering cross section in spherical harmonics,

$$\begin{aligned} \Phi_{p,n} &\equiv \int_{4\pi} d\Omega \Psi(\vec{\Omega}) Y_{p,n}(\vec{\Omega}), \\ \sigma_{s,p} &\equiv \int_{-1}^1 d\mu \sigma_s(\mu) P_p(\mu), \end{aligned} \quad (2.16)$$

where we have used the following relationships:

$$\begin{aligned} \mu &\equiv \vec{\Omega}' \cdot \vec{\Omega}, \\ \sigma_s(\vec{\Omega}' \cdot \vec{\Omega}) &\equiv \frac{1}{2\pi} \sigma_s(\mu), \\ P_p(\vec{\Omega}' \cdot \vec{\Omega}) &\equiv \frac{1}{2\pi} P_p(\mu). \end{aligned} \quad (2.17)$$

Table 2.1: 2D angle mapping from the first quadrant into the other 3 quadrants.

Quadrant	$\mu$	$\eta$
1	$\mu_1 = \mu_1$	$\eta_1 = \eta_1$
2	$\mu_2 = -\mu_1$	$\eta_2 = \eta_1$
3	$\mu_3 = -\mu_1$	$\eta_3 = -\eta_1$
4	$\mu_4 = \mu_1$	$\eta_4 = -\eta_1$

Table 2.2: 3D angle mapping from the first octant into the other 7 octants.

Quadrant	$\mu$	$\eta$	$\xi$
1	$\mu_1 = \mu_1$	$\eta_1 = \eta_1$	$\xi_1 = \xi_1$
2	$\mu_2 = -\mu_1$	$\eta_2 = \eta_1$	$\xi_2 = \xi_1$
3	$\mu_3 = -\mu_1$	$\eta_3 = -\eta_1$	$\xi_3 = \xi_1$
4	$\mu_4 = \mu_1$	$\eta_4 = -\eta_1$	$\xi_4 = \xi_1$
5	$\mu_5 = \mu_1$	$\eta_5 = \eta_1$	$\xi_5 = -\xi_1$
6	$\mu_6 = -\mu_1$	$\eta_6 = \eta_1$	$\xi_6 = -\xi_1$
7	$\mu_7 = -\mu_1$	$\eta_7 = -\eta_1$	$\xi_7 = -\xi_1$
8	$\mu_8 = \mu_1$	$\eta_8 = -\eta_1$	$\xi_8 = -\xi_1$

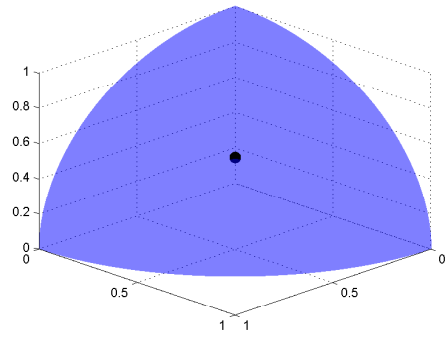
We conclude our discussion of angular discretizations by presenting two common angular quadrature sets that will be employed in this dissertation work. Section 2.3.1 presents the Level Symmetric (LS) quadrature set and Section 2.3.2 presents the Product Gauss-Legendre-Chebyshev (PGLC) quadrature set.

### 2.3.1 Level-Symmetric Quadrature Set

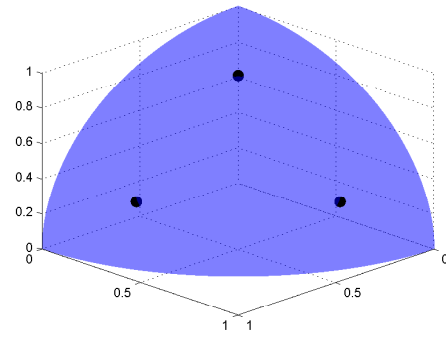
The first quadrature set we present is the common Level Symmetric set.

### 2.3.2 Product Gauss-Legendre-Chebyshev Quadrature Set

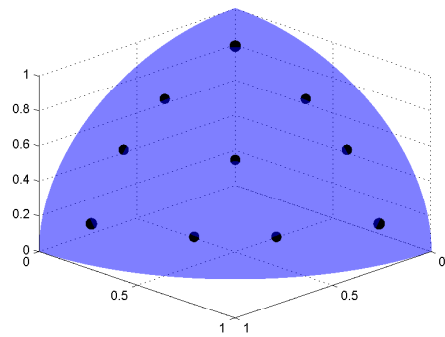
The second angular quadrature set we will present is a Product Gauss-Legendre-Chebyshev (PGLC) set. It is formed by the product-wise multiplication of a Gauss-Chebyshev quadrature in the azimuthal direction and a Gauss-Legendre quadrature



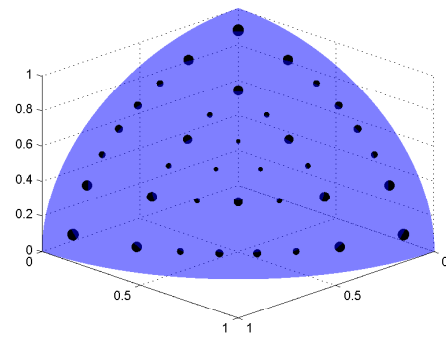
(a)



(b)



(c)



(d)

Figure 2.2: Level-Symmetric angular quadrature set of order (a) 2, (b) 4, (c) 8, and (d) 16.

in the polar direction. It has the following key differences from the Level Symmetric set:

- Does not have  $90^\circ$  rotational invariance within the primary octant; still maintains octant-to-octant symmetry however;
- Has more control over the placement of the angular directions within the primary octant;
- Quadrature weights are aligned with the polar level;
- Has strictly positive weights for all polar and azimuthal combinations.

From the listed differences, we can already discern some clear advantages and disadvantages from a fully-symmetric quadrature set like LS. If a high number of angles are required for a problem, then negative weights do not arise. This is beneficial for transport problems with significant discontinuities. Also, the quadrature directions can be preferentially distributed in the primary octant if required for a particular problem. For example, if the transport solution is smoothly varying in the polar direction and not in the azimuthal direction, then we can specify a larger number of quadrature points in the azimuthal direction, with much fewer points in the polar direction. However, this also highlights the fact that the quadrature weights are aligned with the polar level, which can lead to less accurate moment integrations for certain transport problems.

For this dissertation, we will use the following notation to define the product nature of the PGLC quadrature points:  $S_a^p$ . Here,  $a$  and  $p$  correspond to the number of azimuthal and polar directions in the primary octant, respectively. We demonstrate this definition in Figure 2.3 with several combinations of azimuthal and polar directions. Again, the size of the direction marker corresponds to the relative weight

of quadrature point. One can clearly see that the weights vary on the polar levels and all azimuthal weights on a given polar level are constant.

## 2.4 Spatial Discretization

Using the energy and angular discretizations presented in Sections 2.2 and 2.3, respectively, we write the standard, steady-state, multigroup  $S_N$  transport equation for one angular direction,  $m$ , and one energy group,  $g$ :

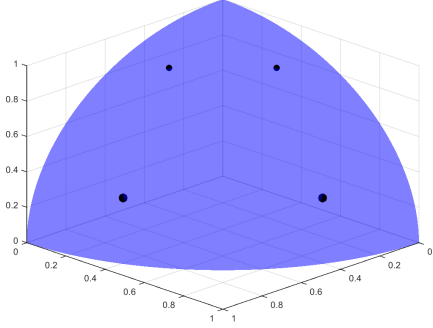
$$\begin{aligned} \left( \vec{\Omega}_m \cdot \vec{\nabla} + \sigma_{t,g} \right) \Psi_{m,g} = & \sum_{g'=1}^G \sum_{p=0}^{N_P} \frac{2p+1}{4\pi} \sigma_{s,p}^{g' \rightarrow g} \sum_{n=-p}^p \Phi_{p,n,g'} Y_{p,n}(\vec{\Omega}_m) \\ & + \frac{\chi_g}{4\pi} \sum_{g'=1}^G \nu \sigma_{f,g'} \Phi_{g'} + Q_{m,g}, \end{aligned} \quad (2.18)$$

where we have dropped the spatial parameter for clarity and is beholden to the following general, discretized boundary condition:

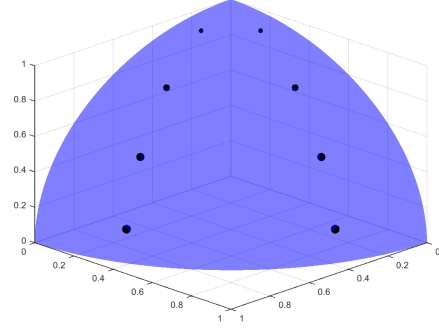
$$\Psi_{m,g}(\vec{r}) = \Psi_{m,g}^{inc}(\vec{r}) + \sum_{g'=1}^G \sum_{\vec{\Omega}_{m'} \cdot \vec{n} > 0} \gamma_{g' \rightarrow g}^{m' \rightarrow m}(\vec{r}) \Psi_{m',g'}(\vec{r}). \quad (2.19)$$

These ( $M \times G$ ) number of discrete, tightly-coupled equations are currently defined as continuous in space.

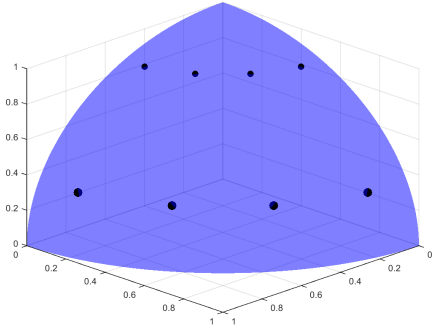
For this dissertation work, we will consider only one type of boundary conditions: Dirichlet-type boundaries (also called *first-type boundary condition* in some physics and mathematical communities). In particular we will only utilize incoming-incident and reflecting boundary conditions which correspond to  $\vec{r} \in \partial\mathcal{D}^d$  and  $\vec{r} \in \partial\mathcal{D}^r$ , respectively. The full domain boundary is then the union:  $\partial\mathcal{D} = \partial\mathcal{D}^d \cup \partial\mathcal{D}^r$ . This leads to the boundary condition being succinctly written for one angular direction,  $m$ , and one energy group,  $g$  as



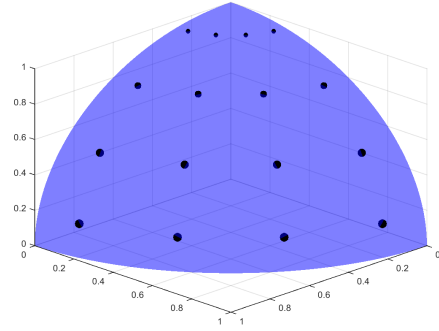
(a)



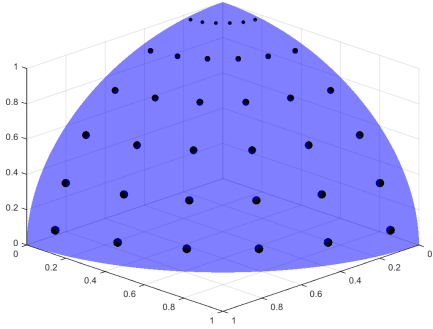
(b)



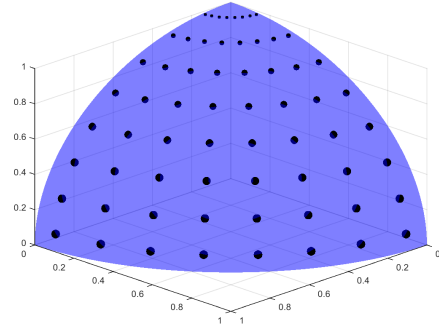
(c)



(d)



(e)



(f)

Figure 2.3: Product Gauss-Legendre-Chebyshev angular quadrature set with orders: (a)  $S_2^2$ , (b)  $S_2^4$ , (c)  $S_4^2$ , (d)  $S_4^4$ , (e)  $S_6^2$ , and (f)  $S_8^2$ .



$$\Psi_{m,g}(\vec{r}) = \begin{cases} \Psi_{m,g}^{inc}(\vec{r}), & \vec{r} \in \partial\mathcal{D}^d \\ \Psi_{m',g}(\vec{r}), & \vec{r} \in \partial\mathcal{D}^r \end{cases} \quad (2.20)$$

where the reflecting angle is  $\vec{\Omega}_{m'} = \vec{\Omega}_m - 2(\vec{\Omega}_m \cdot \vec{n})\vec{n}$  and  $\vec{n}$  is oriented outward from the domain. To properly utilize the reflecting boundary condition that we have proposed, the angular quadrature set defined in Section 2.3 needs the following properties.

1. The reflected directions,  $\vec{\Omega}_{m'}$ , are also in the quadrature set for all  $\vec{r} \in \partial\mathcal{D}^r$ .
2. The weights of the incident,  $w_m$ , and reflected,  $w_{m'}$ , angles must be equal.

For problems where the reflecting boundaries align with the  $x, y, z$  axes, this will not be an issue with standard quadrature sets (*e.g.* level-symmetric or Gauss-Legendre-Chebyshev). However, if the reflecting boundaries do not align in this manner, then additional care must be employed in calculating appropriate angular quadrature sets.

For the spatial discretization of the problem domain, we simplify Eq. (2.18) into a single energy group and drop the fission term (it can be lumped into the 0th order external source term and will act similarly to the total interaction term)

$$\vec{\Omega}_m \cdot \vec{\nabla} \Psi_m + \sigma_t \Psi_m = \sum_{p=0}^{N_P} \frac{2p+1}{4\pi} \sum_{n=-p}^p Y_{p,n}(\vec{\Omega}_m) [\sigma_{s,p} \Phi_{p,n} + Q_{p,n}] \quad (2.21)$$

to form  $M$  ( $m = 1, \dots, M$ ) angularly discrete equations. We then lay down an unstructured mesh  $\mathcal{T}_h \in \mathbb{R}^d$ , over the spatial domain, where  $d$  is the dimensionality of the problem ( $d = 1, 2, 3$ ). This mesh consists of non-overlapping spatial elements to form a complete union over the entire spatial domain:  $\mathcal{D} = \bigcup_{K \in \mathcal{T}_h} K$ . To form

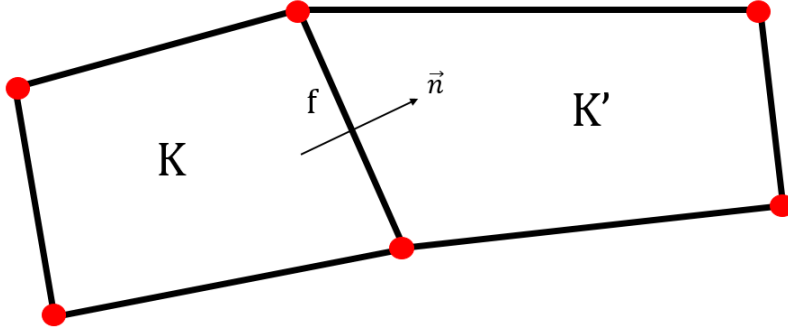


Figure 2.4: Two cells of the spatial discretization with the connecting face,  $f$ , with normal direction,  $\vec{n}$ , oriented from cell  $K$  to cell  $K'$ .

the DGFEM set of equations [7, 8], we consider a spatial cell  $K \in \mathbb{R}^d$  which has  $N_V^K$  vertices and  $N_f^K$  faces. Each face of cell  $K$  resides in dimension  $\mathbb{R}^{d-1}$  and is formed by a connection of a subset of vertices. For a 1D problem, each face is a single point. For a 2D problem, each face is a line segment connecting two distinct points. For a 3D problem, each face is a  $\mathbb{R}^2$  closed polygon (not necessarily coplanar) which may or not be convex. An example of this interconnection between elements is given for a  $\mathbb{R}^2$  problem in Figure 2.4 between our cell of interest,  $K$ , and another cell,  $K'$ , separated by the face  $f$ . We have chosen the normal direction of the face to have orientation from cell  $K$  to cell  $K'$  while we form the DGFEM equations for cell  $K$ . This means that if we were instead analyzing cell  $K'$ , then the face  $f$  normal,  $\vec{n}'$ , would be opposite (*i.e.*  $\vec{n}' = -\vec{n}$ ).

Next, we left-multiply Eq. (2.21) by an appropriate test function  $b_m$ , integrate over cell  $K$ , and apply Gauss' Divergence Theorem to the streaming term to obtain the Galerkin weighted-residual for cell  $K$  for an angular direction  $\vec{\Omega}_m$ :

$$\begin{aligned}
& - \left( \vec{\Omega}_m \cdot \vec{\nabla} b_m, \Psi_m \right)_K + \sum_{f=1}^{N_f^K} \left\langle (\vec{\Omega}_m \cdot \vec{n}) b_m, \tilde{\Psi}_m \right\rangle_f + \left( \sigma_t b_m, \Psi_m \right)_K \\
& = \sum_{p=0}^{N_P} \sum_{n=-p}^p \frac{2p+1}{4\pi} Y_{p,n}(\vec{\Omega}_m) \left[ \left( \sigma_{s,p} b_m, \Phi_{p,n} \right)_K + (b_m, Q_{p,n})_K \right].
\end{aligned} \tag{2.22}$$

The cell boundary fluxes,  $\tilde{\Psi}_m$ , will depend on the cell boundary type and will be defined shortly. The cell boundary  $\partial\mathcal{D}_K = \bigcup_{f \in N_f^K} f$  is the closed set of the  $N_f^K$  faces of the geometric cell. The inner products:

$$(f, g)_K \equiv \int_K f g \, dr \tag{2.23}$$

and

$$\langle f, g \rangle_f \equiv \int_f f g \, ds \tag{2.24}$$

correspond to integrations over the cell and faces, respectively, where  $dr \in \mathbb{R}^d$  is within the cell and  $ds \in \mathbb{R}^{d-1}$  is along the cell boundary. We note that we will use this notation of the inner product for the remainder of the dissertation unless otherwise stated. We then separate the summation of the cell  $K$  boundary integration terms into two different types: outflow boundaries ( $\partial K^+ = \{\vec{r} \in \partial K : \vec{n}(\vec{r}) \cdot \vec{\Omega}_m > 0\}$ ) and inflow boundaries ( $\partial K^- = \{\vec{r} \in \partial K : \vec{n}(\vec{r}) \cdot \vec{\Omega}_m < 0\}$ ). The inflow boundaries can further be separated into inflow from another cell:  $\partial K^- \setminus \partial\mathcal{D}$ ; inflow from incident flux on the domain boundary:  $\partial K^- \cap \partial\mathcal{D}^d$ ; and reflecting domain boundaries:  $\partial K^- \cap \partial\mathcal{D}^r$ . At this point, we note that the derivation can comprise an additional step by using Gauss' Divergence Theorem again on the streaming term. This is sometimes performed for radiation transport work but we will not do so here. Therefore, with

the cell boundary terminology as proposed, Eq. (2.22) can be written into the following form:

$$\begin{aligned}
& - \left( \vec{\Omega}_m \cdot \vec{\nabla} b_m, \Psi_m \right)_K + \left( \sigma_t b_m, \Psi_m \right)_K \\
& + \left\langle (\vec{\Omega}_m \cdot \vec{n}) b_m, \tilde{\Psi}_m \right\rangle_{\partial K^+} + \left\langle (\vec{\Omega}_m \cdot \vec{n}) b_m, \tilde{\Psi}_m \right\rangle_{\partial K^- \setminus \partial \mathcal{D}} \\
& + \left\langle (\vec{\Omega}_m \cdot \vec{n}) b_m, \tilde{\Psi}_m \right\rangle_{\partial K^- \cap \partial \mathcal{D}^d} + \left\langle (\vec{\Omega}_m \cdot \vec{n}) b_m, \tilde{\Psi}_m \right\rangle_{\partial K^- \cap \partial \mathcal{D}^r} . \\
& = \sum_{p=0}^{N_F} \sum_{n=-p}^p \frac{2p+1}{4\pi} Y_{p,n}(\vec{\Omega}_m) \left[ \left( \sigma_{s,p} b_m, \Phi_{p,n} \right)_K + (b_m, Q_{p,n})_K \right]
\end{aligned} \tag{2.25}$$

We can now deal with the boundary fluxes,  $\tilde{\Psi}_m$ , by enforcing the ubiquitously-used *upwind scheme*. In simple nomenclature, the upwind scheme corresponds to using the angular flux values within the cell for outflow boundaries and angular flux values outside the cell for inflow boundaries. Mathematically, the upwind scheme can succinctly be written as the following for all boundary types,

$$\tilde{\Psi}_m(\vec{r}) = \begin{cases} \Psi_m^-, & \partial K^+ \\ \Psi_m^+, & \partial K^- \setminus \partial \mathcal{D} \\ \Psi_m^{inc}, & \partial K^- \cap \partial \mathcal{D}^d \\ \Psi_m^-, & \partial K^- \cap \partial \mathcal{D}^r \end{cases}, \tag{2.26}$$

when the following trace is applied to the angular fluxes :

$$\Psi_m^\pm(\vec{r}) \equiv \lim_{s \rightarrow 0^\pm} \Psi_m \left( \vec{r} + s(\vec{\Omega}_m \cdot \vec{n}) \vec{n}_m \right). \tag{2.27}$$

This trace has the notation, with  $\vec{n}$  pointing outwards from cell  $K$ , of  $\Psi_m^-$  corresponding to fluxes within the cell and  $\Psi_m^+$  corresponding to fluxes out of the cell. Now, using the upwind scheme as previously defined, we can write our complete set

of DGFEM equations for cell  $K$  as

$$\begin{aligned}
& -\left(\vec{\Omega}_m \cdot \vec{\nabla} b_m, \Psi_m\right)_K + \left(\sigma_t b_m, \Psi_m\right)_K + \left\langle (\vec{\Omega}_m \cdot \vec{n}) b_m, \Psi_m^- \right\rangle_{\partial K^+} \\
& + \left\langle (\vec{\Omega}_m \cdot \vec{n}) b_m, \Psi_m^+ \right\rangle_{\partial K^- \setminus \partial \mathcal{D}} + \left\langle (\vec{\Omega}_m \cdot \vec{n}) b_m, \Psi_{m'}^- \right\rangle_{\partial K^- \cap \partial \mathcal{D}^r} \\
& = \sum_{p=0}^{N_P} \sum_{n=-p}^p \frac{2p+1}{4\pi} Y_{p,n}(\vec{\Omega}_m) \left[ \left(\sigma_{s,p} b_m, \Phi_{p,n}\right)_K + (b_m, Q_{p,n})_K \right] \\
& + \left\langle (\vec{\Omega}_m \cdot \vec{n}) b_m, \Psi_m^{inc} \right\rangle_{\partial K^- \cap \partial \mathcal{D}^d}
\end{aligned} \tag{2.28}$$

We note that fluxes without the trace superscript are all within the cell. By completely defining our mathematical formulation for an arbitrary spatial cell, it is easy to see that the full set of equations to define our discretized solution space for a single angle and energy group comprises of a simple double integration loop. The full set of equations can be formed by looping over all spatial cells,  $\mathcal{D} = \bigcup_{K \in \mathcal{T}_h} K$ , while further looping over all faces within each cell,  $\partial \mathcal{D}_K = \bigcup_{f \in N_f^K} f$ . Section 2.5 will further detail how all the DGFEM equations are formed along with efficient solution methods. We conclude this section by defining the elementary matrix terms for a given cell as follows.

#### 2.4.1 Elementary Mass Matrices

In the spatially discretized equations presented in Section 2.4, there are several reaction terms that appear with the form:  $\left(\sigma b_m, \Psi_m\right)_K$  for a given angular direction,  $m$ , and for a spatial cell,  $K$ . In FEM analysis these reaction terms are ubiquitously referred to as the mass matrix terms [9, 10]. For cell  $K$ , we define the elementary mass matrix,  $\mathbf{M}$  as

$$\mathbf{M}_K = \int_K \mathbf{b}_K \mathbf{b}_K^T d\vec{r}, \tag{2.29}$$

where  $\mathbf{b}_K$  corresponds to the set of  $N_K$  basis functions that have non-zero measure in cell  $K$ . Depending on the FEM basis functions utilized, the integrals in Eq. (2.29) can be directly integrated analytically. However, if in general, the basis functions cannot be analytically integrated on an arbitrary set of cell shapes, then a numerical integration scheme becomes necessary. If we define a quadrature set,  $\{\vec{x}_q, w_q^K\}_{q=1}^{N_q}$ , for cell  $K$ , consisting of  $N_q$  points,  $\vec{x}_q$ , and weights,  $w_q^K$ , then we can numerically calculate the mass matrix by the following

$$\mathbf{M}_K = \sum_{q=1}^{N_q} w_q^K \mathbf{b}_K(\vec{x}_q) \mathbf{b}_K^T(\vec{x}_q). \quad (2.30)$$

In this case, it is necessary that the sum of the weights of this quadrature set exactly equal the geometric measure of cell  $K$ . This means that  $\sum_{q=1}^{N_q} w_q^K$  is equal to the cell width in 1 dimension, the cell area in 2 dimensions, and the cell volume in 3 dimensions.

Since  $\mathbf{b}_K$  consists of a column vector for the basis functions and  $\mathbf{b}_K^T$  consists of a row vector, then their multiplication will obviously yield a full ( $N_K \times N_K$ ) matrix. This matrix is written for completeness of this discussion on the mass matrix:

$$\mathbf{M}_K = \begin{bmatrix} \int_K b_1 b_1 & \dots & \int_K b_1 b_j & \dots & \int_K b_1 b_{N_K} \\ \vdots & & \vdots & & \vdots \\ \int_K b_i b_1 & \dots & \int_K b_i b_j & \dots & \int_K b_i b_{N_K} \\ \vdots & & \vdots & & \vdots \\ \int_K b_{N_K} b_1 & \dots & \int_K b_{N_K} b_j & \dots & \int_K b_{N_K} b_{N_K} \end{bmatrix}, \quad (2.31)$$

where an individual matrix entry is of the form:

$$M_{i,j}^K = \int_K b_i b_j. \quad (2.32)$$

### 2.4.2 Elementary Streaming Matrices

Next, we will consider the streaming term that has the form:  $(\vec{\Omega}_m \cdot \vec{\nabla} b_m, \Psi_m)_K$  for a given angular direction,  $m$ , and for a spatial cell,  $K$ .  $\vec{\nabla}$  is the gradient operator in physical space. It has the form of  $\vec{\nabla} = \left[ \frac{d}{dx} \right]$  in 1 dimension, the form of  $\vec{\nabla} = \left[ \frac{\partial}{\partial x}, \frac{\partial}{\partial y} \right]$  in 2 dimensions, and the form of  $\vec{\nabla} = \left[ \frac{\partial}{\partial x}, \frac{\partial}{\partial y}, \frac{\partial}{\partial z} \right]$  in 3 dimensions. Since for every cell, the streaming term is applied for all  $M$  angles in the angular discretization, we define the analytical elementary streaming matrix:

$$\vec{\mathbf{G}}_K = \int_K \vec{\nabla} \mathbf{b}_K \mathbf{b}_K^T d\vec{r}, \quad (2.33)$$

which has dimensionality  $(N_K \times N_K \times d)$ . We choose to store the elementary streaming matrix in this form and not store  $M$  separate  $(N_K \times N_K)$  local matrices corresponding to the application of the dot product  $(\vec{\Omega}_m \cdot \int_K \vec{\nabla} \mathbf{b}_K \mathbf{b}_K^T d\vec{r})$ . Instead we simply evaluate the dot product with the appropriate angular direction whenever necessary. This has great benefit when trying to run large transport problems when memory becomes a premium and processor operations are not our limiting bottleneck.

Just like the elementary mass matrix, we can use the same spatial quadrature set,  $\left\{ \vec{x}_q, w_q^K \right\}_{q=1}^{N_q}$ , for cell  $K$  to numerically calculate the streaming matrix:

$$\vec{\mathbf{G}}_K = \sum_{q=1}^{N_q} w_q^K \vec{\nabla} \mathbf{b}_K(\vec{x}_q) \mathbf{b}_K^T(\vec{x}_q). \quad (2.34)$$

In this case, this local cell-wise streaming matrix has the full matrix form:

$$\vec{\mathbf{G}}_K = \begin{bmatrix} \int_K \vec{\nabla} b_1 b_1 & \dots & \int_K \vec{\nabla} b_1 b_j & \dots & \int_K \vec{\nabla} b_1 b_{N_K} \\ \vdots & & \vdots & & \vdots \\ \int_K \vec{\nabla} b_i b_1 & \dots & \int_K \vec{\nabla} b_i b_j & \dots & \int_K \vec{\nabla} b_i b_{N_K} \\ \vdots & & \vdots & & \vdots \\ \int_K \vec{\nabla} b_{N_K} b_1 & \dots & \int_K \vec{\nabla} b_{N_K} b_j & \dots & \int_K \vec{\nabla} b_{N_K} b_{N_K} \end{bmatrix}, \quad (2.35)$$

where an individual matrix entry is of the form:

$$\vec{G}_{i,j}^K = \int_K \vec{\nabla} b_i b_j. \quad (2.36)$$

### 2.4.3 Elementary Surface Matrices

Finally, the last terms to consider of the discretized transport equation are those found on the faces of the cell boundary:  $\vec{\Omega}_m \cdot \langle \vec{n} b_m, \Psi_m \rangle_{\partial K}$ . These terms are analagous to the cell mass matrix but are computed on the cell boundary with dimensionality  $(d - 1)$ .

## 2.5 Solution Procedures

To this point, we have properly described the procedures to discretize the transport problem in energy, angle, and space. We now spend the remainder of this chapter discussing various methodologies to efficiently solve the tightly-coupled system of equations composing our transport problem. Section 2.5.1



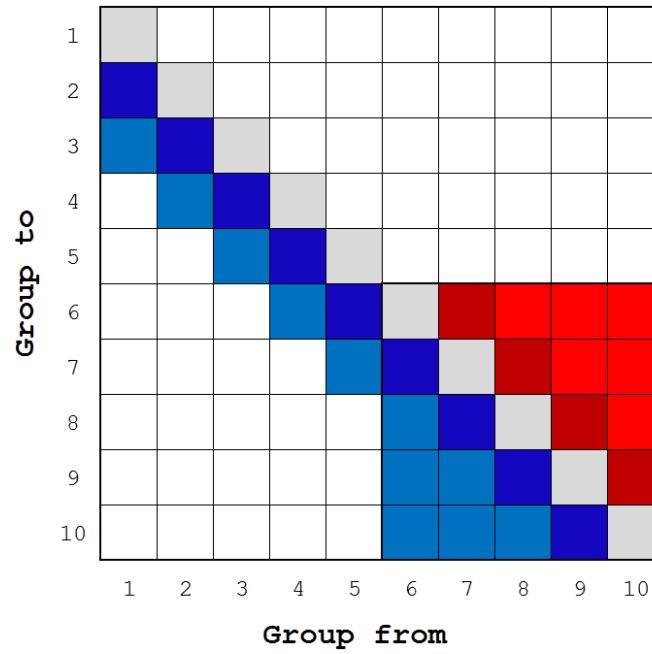
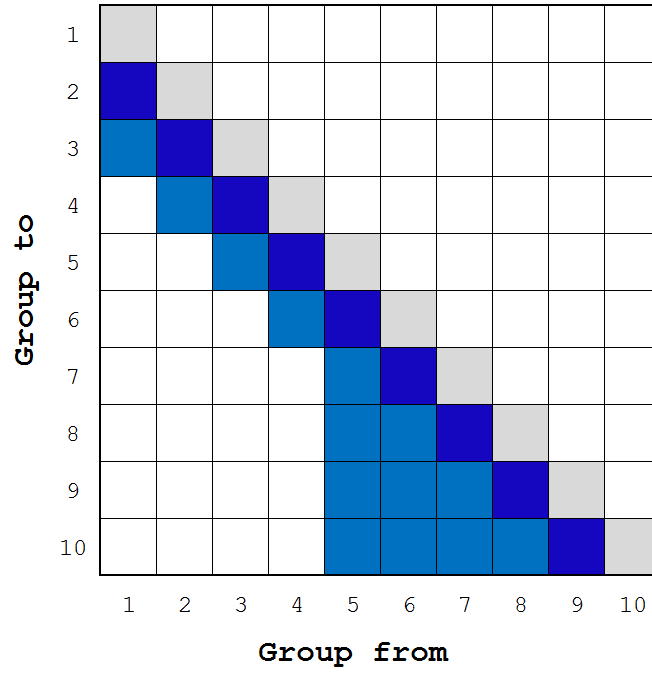


Figure 2.5: Scattering matrices (top) without and (bottom) with upscattering. The gray corresponds to within-group scattering; the blue corresponds to down-scattering in energy; and the red corresponds to up-scattering in energy.

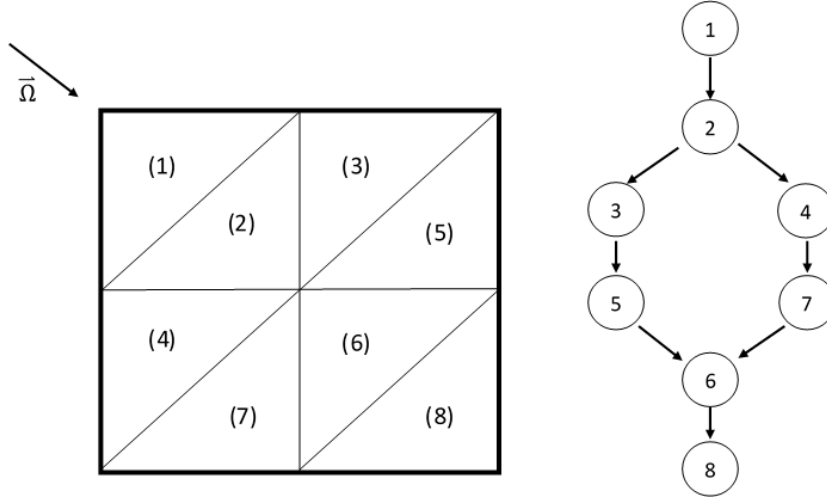


Figure 2.6: blah.

### 2.5.1 Angle and Energy Iteration Procedures

#### 2.5.1.1 Source Iteration

#### 2.5.1.2 Krylov Subspace Methods - GMRES

### 2.5.2 Spatial Solution Procedures

#### Section 2.5.1

#### 2.5.2.1 Transport Sweeping

#### 2.5.2.2 Adaptive Mesh Refinement Procedures

## 2.6 Conclusions

In this chapter, we have presented the tightly-coupled system of equations that comprise the DGFEM  $S_N$  transport equation.

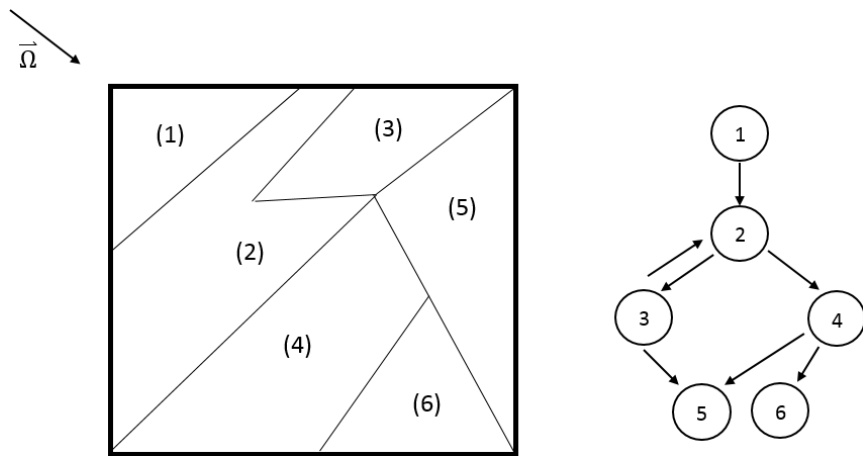


Figure 2.7: blah.

### 3. FEM BASIS FUNCTIONS FOR UNSTRUCTURED POLYTOPES

discuss benefits/desires here and some history...

#### 3.1 Linear Basis Functions on 2D Polygons

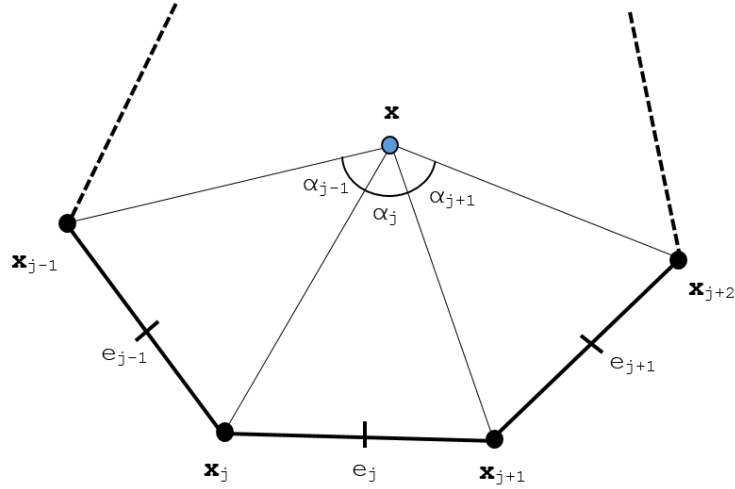


Figure 3.1: Arbitrary polygon with geometric properties used for 2D basis function generation.

In this dissertation, all 1st-order, two-dimensional basis functions for a cell will obey the properties for barycentric coordinates. They will form a *partition of unity*,

$$\sum_{i=1}^{N_K} b_i(\vec{x}) = 1; \quad (3.1)$$

coordinate interpolation will result from an *affine combination* of the vertices,

$$\sum_{i=1}^{N_K} b_i(\vec{x}) \vec{x}_i = \vec{x}; \quad (3.2)$$

and they will satisfy the *Lagrange property*,

$$b_i(\vec{x}_j) = \delta_{ij}. \quad (3.3)$$

$N_K$  is again the number of spatial degrees with measure in element  $K$ . Using the *partition of unity* of Eq. (3.1), we can rewrite Eqs. (3.1-3.2) into a separate, compact, vectorized form for completeness

$$\sum_{i=1}^{N_K} b_i(\vec{x}) \vec{c}_{i,1}(\vec{x}) = \vec{q}_1, \quad (3.4)$$

where  $\vec{c}_{i,1}(\vec{x})$  and  $\vec{q}_1$  are the lineary-complete constraint and equivalence terms, respectively. These terms are simply:

$$\vec{c}_{i,1}(\vec{x}) = \begin{bmatrix} 1 \\ x_i - x \\ y_i - y \end{bmatrix} \quad \text{and} \quad \vec{q}_1 = \begin{bmatrix} 1 \\ 0 \\ 0 \end{bmatrix}, \quad (3.5)$$

respectively.

### 3.1.1 Traditional Linear Basis Functions - $\mathbb{P}_1$ and $\mathbb{Q}_1$ Spaces

Before presenting basis function sets applicable to polytope finite elements, we first provide two common basis functions that are exact on triangles and convex quadrilaterals: the  $\mathbb{P}_1$  and  $\mathbb{Q}_1$  spaces, respectively.

$$\begin{aligned} b_1(r, s) &= 1 - r - s \\ b_2(r, s) &= r \\ b_3(r, s) &= s \end{aligned} \quad (3.6)$$

and

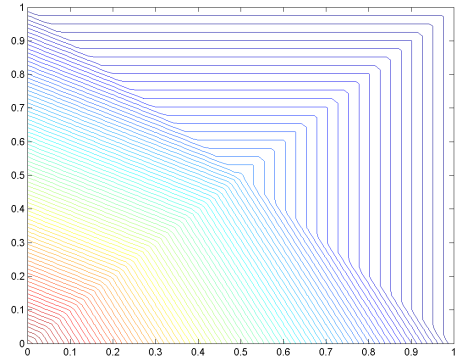
$$\begin{aligned}
b_1(r, s) &= (1 - r)(1 - s) \\
b_2(r, s) &= r(1 - s) \\
b_3(r, s) &= rs \\
b_4(r, s) &= (1 - r)s
\end{aligned} \tag{3.7}$$

### 3.1.2 Wachspress Rational Basis Functions

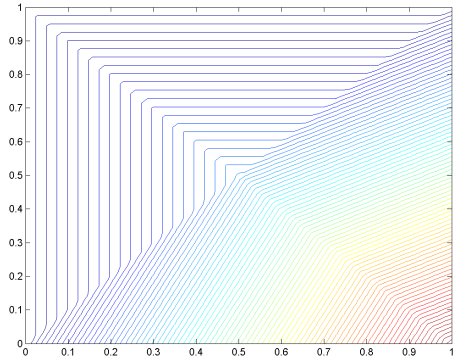
### 3.1.3 Piecewise Linear (PWL) Basis Functions

$$b_j(x, y) = t_j(x, y) + \alpha_j^K t_c(x, y) \tag{3.8}$$

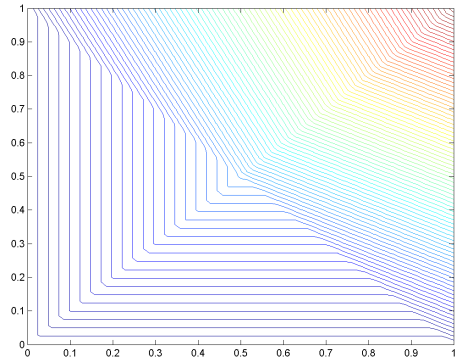
$t_j$  is the standard 2D linear function with unity at vertex  $j$  that linearly decreases to zero to the cell center and each adjoining vertex.  $t_c$  is the 2D cell “tent” function which is unity at the cell center and linearly decreases to zero to each cell vertex.  $\alpha_j^K$  is the weight parameter for vertex  $j$  in cell  $K$ .



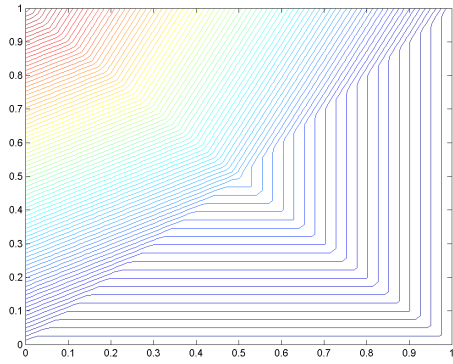
(a)



(b)



(c)



(d)

Figure 3.2: Contour plots of the PWL basis functions on the unit square for the vertices located at: (a) (0,0), (b) (1,0), (c) (1,1), and (d) (0,1).

### 3.1.4 Mean Value Basis Functions

### 3.1.5 Maximum Entropy Basis Functions

### 3.1.6 Summary of 2D Linear Basis Functions on Polygons

## 3.2 Quadratic Serendipity Basis Functions on 2D Polygons

### 3.2.1 Traditional Quadratic Basis Functions - $\mathbb{P}_2$ and $\mathbb{S}_2$ Spaces

### 3.2.2 Quadratic Mean Value Coordinates on 2D Polygons

### 3.2.3 Quadratic Maximum Entropy Coordinates on 2D Polygons

## 3.3 Linear Basis Functions on 3D Polyhedra

### 3.3.1 3D Linear and TriLinear Basis Functions

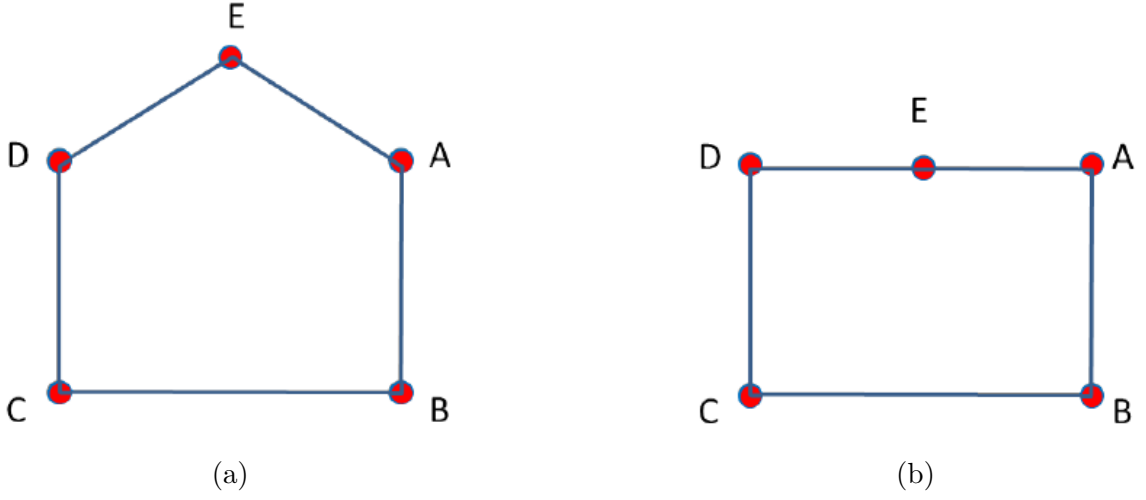


Figure 3.3: Vertex structure for a (a) regular pentagonal cell and a (b) degenerate pentagonal cell.

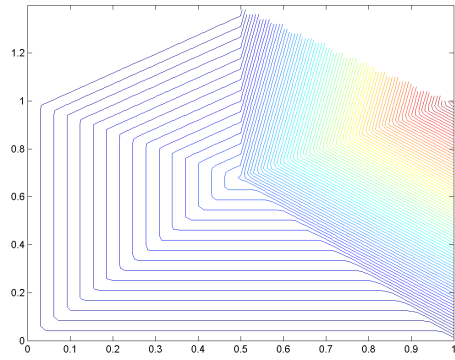
and

$$\begin{aligned}
 b_1(r, s, t) &= (1 - r)(1 - s)(1 - t) \\
 b_2(r, s, t) &= r(1 - s)(1 - t) \\
 b_3(r, s, t) &= rs(1 - t) \\
 b_4(r, s, t) &= (1 - r)s(1 - t) \\
 b_5(r, s, t) &= (1 - r)(1 - s)t \\
 b_6(r, s, t) &= r(1 - s)t \\
 b_7(r, s, t) &= rst \\
 b_8(r, s, t) &= (1 - r)st
 \end{aligned} \tag{3.10}$$

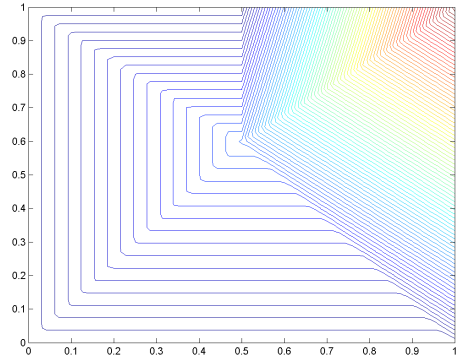
### 3.3.2 3D Piecewise Linear (PWL) Basis Functions

The 3D PWL basis functions share a similar form to the 2D PWL basis functions.

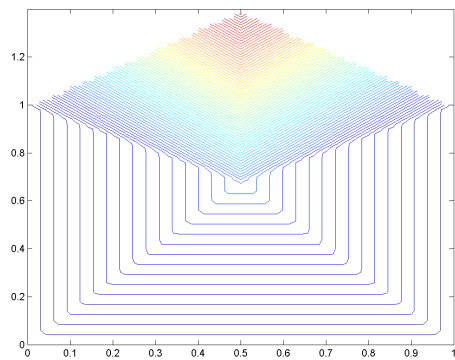




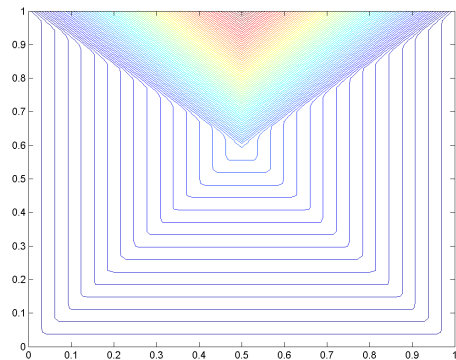
(a)



(b)

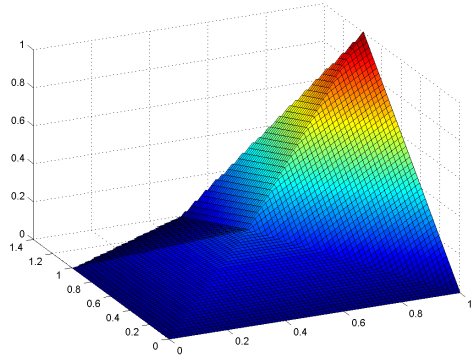


(c)

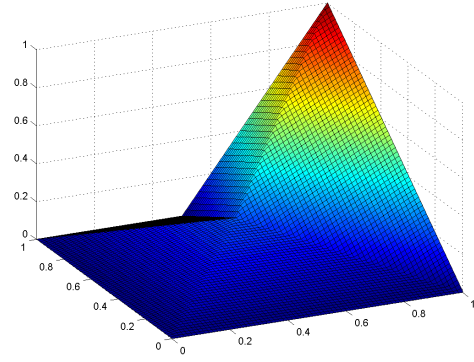


(d)

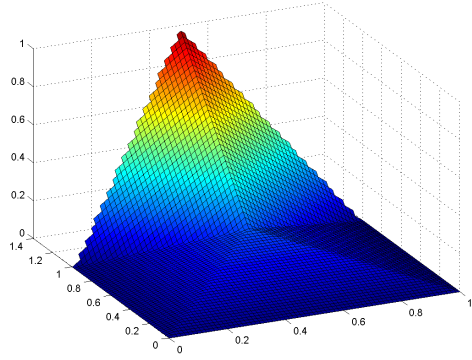
Figure 3.4: Contour plots of the PWL basis functions for a regular pentagon: (a) and (c) as well as a degenerate pentagon: (b) and (d).



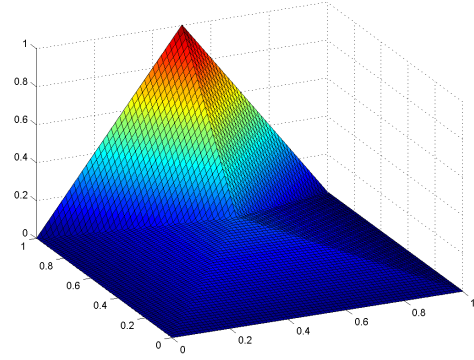
(a)



(b)

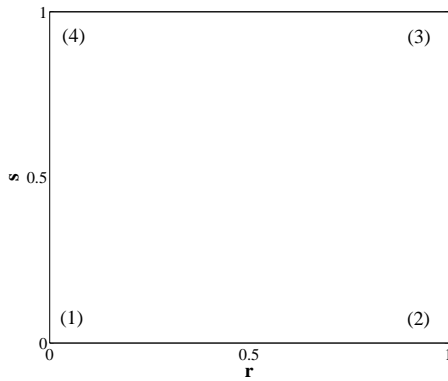


(c)

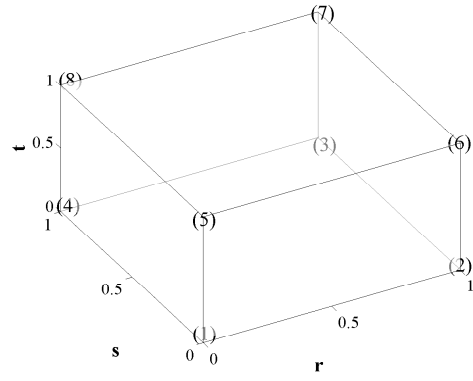


(d)

Figure 3.5: Plots of the PWL basis functions for a regular pentagon: (a) and (c) as well as a degenerate pentagon: (b) and (d).



(a)



(b)

Figure 3.6: Vertex structure for the (a) unit square and (b) unit cube.

$$b_j(x, y, z) = t_j(x, y, z) + \sum_{f=1}^{F_j} \beta_f^j t_f(x, y, z) + \alpha_j^K t_c(x, y, z) \quad (3.11)$$

$t_j$  is the standard 3D linear function with unity at vertex  $j$  that linearly decreases to zero to the cell center, the face center for each face that includes vertex  $j$ , and each vertex that shares an edge with vertex  $j$ .  $t_c$  is the 3D cell “tent” function which is unity at the cell center and linearly decreases to zero to each cell vertex and face center.  $t_f$  is the face “tent” function which is unity at the face center and linearly decreases to zero at each vertex on that face and the cell center.  $\beta_{f,j}$  is the weight parameter for face  $f$  touching cell vertex  $j$ , and  $F_j$  is the number of faces touching vertex  $j$ . Like the previous work defining the PWLD method [11], we also choose to assume the cell and face weighting parameters are

$$\alpha_{K,j} = \frac{1}{N_K} \quad \text{and} \quad \beta_{f,j} = \frac{1}{N_f}, \quad (3.12)$$

respectively, where  $N_K$  is the number of vertices in cell  $K$  and  $N_f$  is the number of vertices on face  $f$ , which leads to constant values of  $\alpha$  and  $\beta$  for each cell and face, respectively. This assumption of the cell weight function holds for both 2D and 3D.

### 3.4 Numerical Results

Now that we have presented several linear polygonal finite element basis sets along with the methodology to convert them to quadratic serendipity-like basis, we present several numerical problems to demonstrate our methodology. First, we demonstrate that the presented basis sets can capture an exactly-linear transport solution in Section 3.4.1. Next, we present some convergence properties of the basis sets using the method of manufactured solutions (MMS) in Section 3.4.2. We then present a searchlight problem and observe how the basis sets react with adaptive mesh

refinement (AMR) to mitigate numerical dispersion through a vacuum in Section 3.4.3.

#### 3.4.1 Two-Dimensional Exactly-Linear Transport Solutions

We present our first numerical example by demonstrating that the linear and quadratic polygonal finite element basis functions capture an exactly-linear solution space. We will show this by the method of exact solutions (MES). Since the coordinate interpolation of the basis functions for the linear basis functions requires exact linear interpolation (Eq. (3.2)), then an exactly-linear solution space can be captured, even on highly distorted polygonal meshes. This also applies to the quadratic serendipity space since it is formed by the product-wise pairings of the linear basis functions. We build our exact solution by investigating the 2D, 1 energy group transport problem with no scattering and an angle-dependent distributed source,

$$\mu \frac{\partial \Psi}{\partial x} + \eta \frac{\partial \Psi}{\partial y} + \sigma_t \Psi = Q(x, y, \mu, \eta), \quad (3.13)$$

where the streaming term was separated into the corresponding two-dimensional terms. We chose to drop the scattering term for this example so that the error arising from iteratively converging our solution would have no impact.

We then define an angular flux solution that is linear in both space and angle along with the corresponding 0th moment scalar flux ( $\Phi_{0,0} \rightarrow \Phi$ ) solution:

$$\begin{aligned} \Psi(x, y, \mu, \eta) &= ax + by + c\mu + d\eta + e \\ \Phi(x, y) &= 2\pi (ax + by + e) \end{aligned} \quad (3.14)$$

One can immediately notice that our 0th moment solution is not dependent on angle. We arrive at this solution by enforcing our 2D angular quadrature set to have the following properties:

$$\sum_q w_q = 2\pi \quad \text{and} \quad \sum_q w_q \begin{bmatrix} \mu_q \\ \eta_q \end{bmatrix} = \begin{bmatrix} 0 \\ 0 \end{bmatrix}. \quad (3.15)$$

Our boundary conditions for all inflow boundaries are then uniquely determined by the angular flux solution of Eq. (3.14). Inserting the angular flux solution of Eq. (3.14) into Eq. (3.13), we obtain the distributed source that will produce our exactly-linear solution space:

$$Q(x, y, \mu, \eta) = a\mu + b\eta + \sigma_t (c\mu + d\eta) + \sigma_t (ax + by + e). \quad (3.16)$$

It is noted that the angular dependence of the source can be removed (which can ease the code development burden) if one sets

$$\begin{aligned} a &= -c\sigma_t, \\ b &= -d\sigma_t. \end{aligned} \quad (3.17)$$

For this example, we test the various 2D polygonal finite element basis functions on six different mesh types. These mesh types include triangular, quadrilateral, and polygonal meshes:

1. Orthogonal cartesian mesh formed by the intersection of 11 equally-spaced vertices in both the  $x$  and  $y$  dimensions. This forms a 10x10 array of quadrilateral mesh cells.
2. Ordered-triangular mesh formed by the bisection of the previous orthogonal cartesian mesh (forming 200 triangles all of the same size/shape).
3. Quadrilateral shestakov grid formed by the randomization of vertices based on a skewness parameter [12, 13]. With a certain range of this skewness parameter,

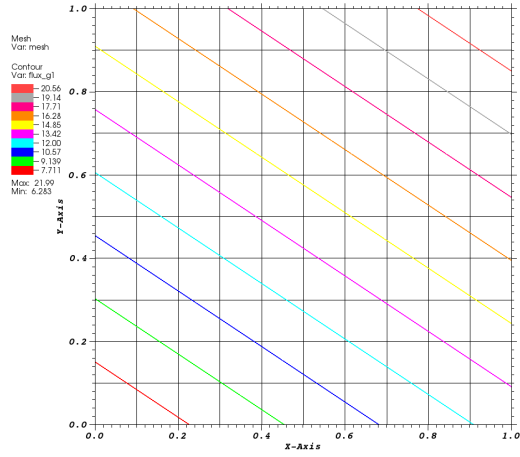
highly distorted meshes can be generated.

4. Sinusoidal polygonal grid that is generated by the transformation of a uniform orthogonal grid based on a sinusoid functional. The transformed vertices are then converted into a polygonal grid by computing a bounded Voronoi diagram.
5. Kershaw’s quadrilateral z-mesh [14]. This mesh is formed by taking an orthogonal quadrilateral grid and displacing certain interior vertices only in the  $y$  dimension.
6. A polygonal variant of the quadrilateral z-mesh. The polygonal grid is formed in a similar manner to the sinusoidal polygonal mesh with a Voronoi diagram.

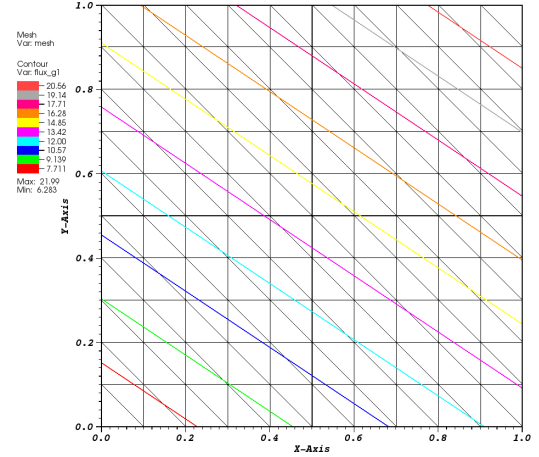
We also wish that both the angular flux solution as well as the 0th moment solution are strictly positive everywhere. Therefore, we set the function parameters in Eq. (3.14) to  $\sigma_t = a = c = d = e = 1.0$  and  $b = 1.5$ . We gave the solution the 40% tilt in space ( $a \neq b$ ) so that it would not align with the triangular mesh. Using an S8 LS quadrature set, we ran all combinations of the polygonal basis functions and the mesh types. The linear solutions for the Wachspress, PWL, mean value, linear maximum entropy, and quadratic serendipity maximum entropy basis functions are presented in Figures 3.7, 3.8, 3.9, 3.10, and 3.11, respectively. We can see that for all the polygonal basis functions, an exact linear solution is captured as shown by the unbroken nature of the contour lines. This even holds on the highly distorted quadrilateral shestakov mesh.

### *3.4.2 Convergence Rate Analysis by the Method of Manufactured Solutions*

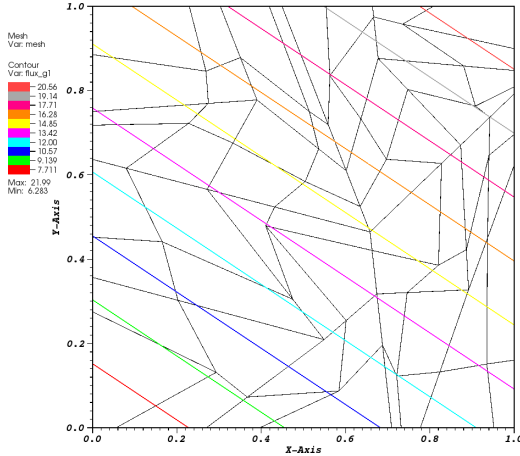
The next numerical example we investigate involves calculating the convergence rate of the solution error via the method of manufactured solutions (MMS). Like MES, MMS enforces a given solution by use of a derived functional form for the



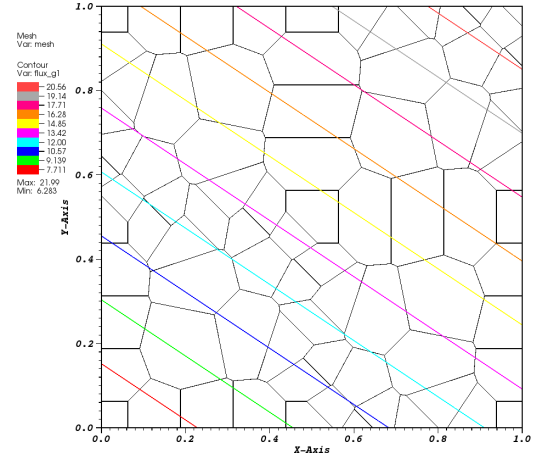
(a)



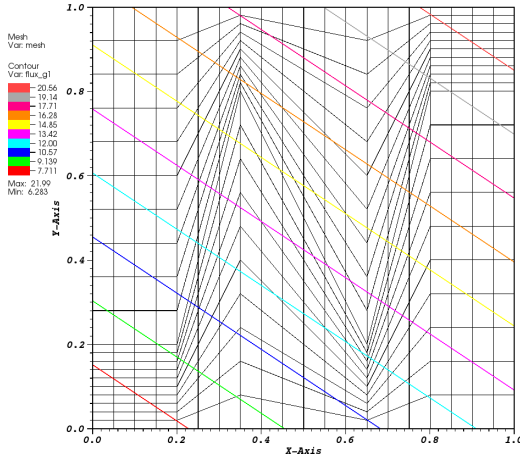
(b)



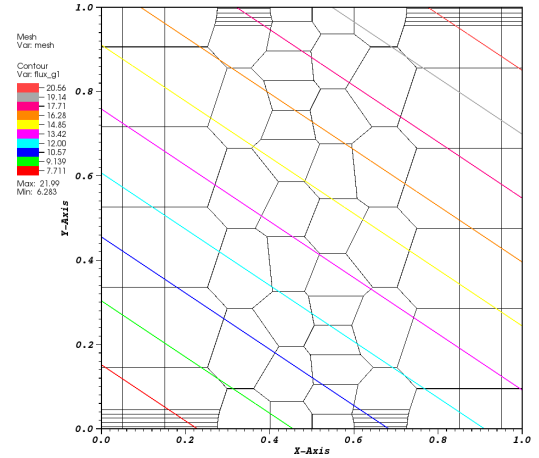
(c)



(d)

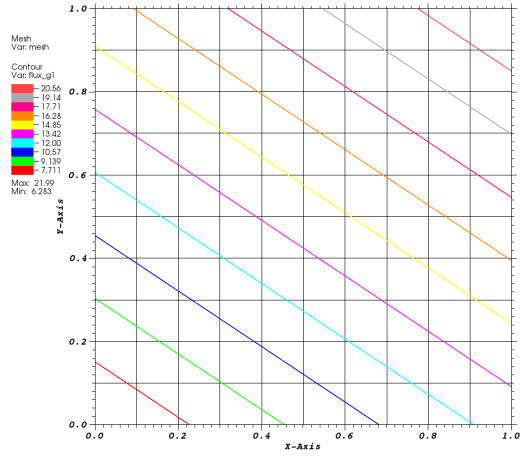


(e)

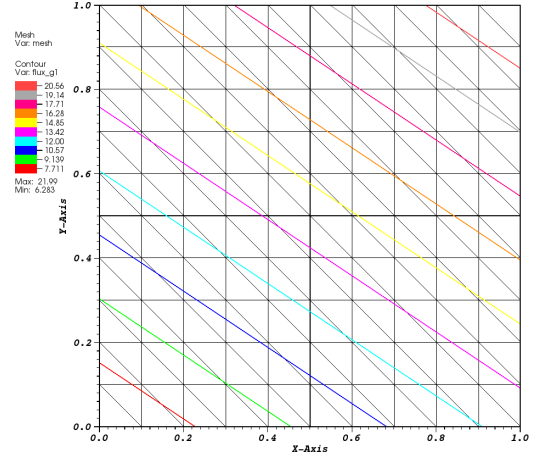


(f)

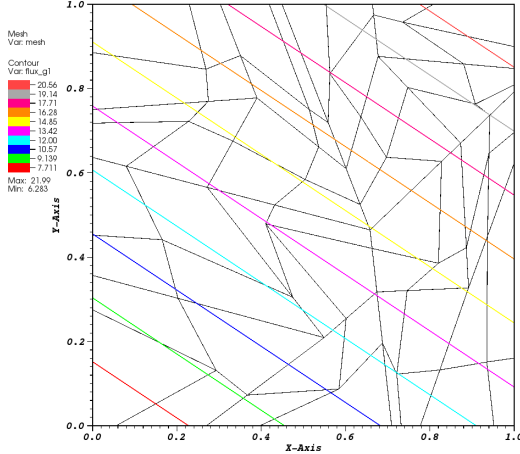
Figure 3.7: Contour plots of the exactly-linear solution with the Wachspress basis functions on (a) cartesian mesh, (b) ordered-triangular mesh, (c) quadrilateral shestakov mesh, (d) sinusoidal polygonal mesh, (e) quadrilateral z-mesh, and (f) polygonal z-mesh.



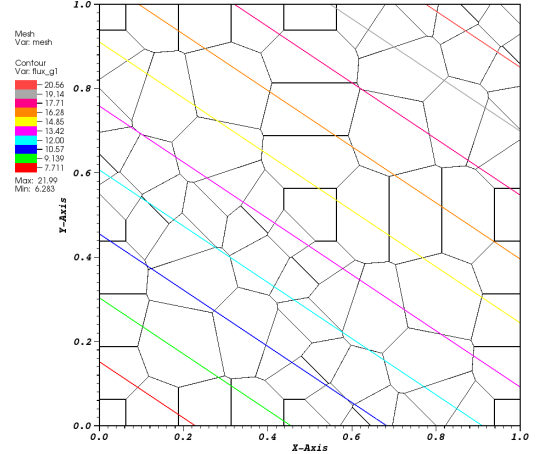
(a)



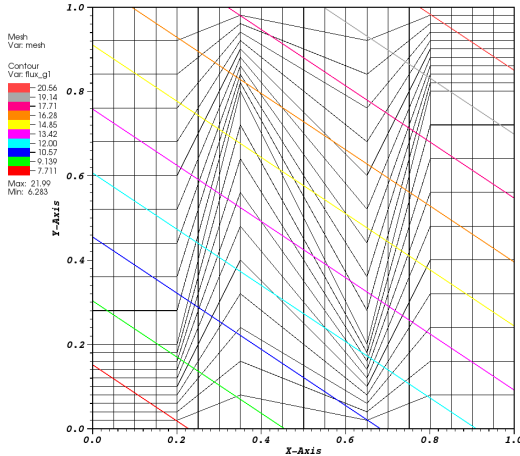
(b)



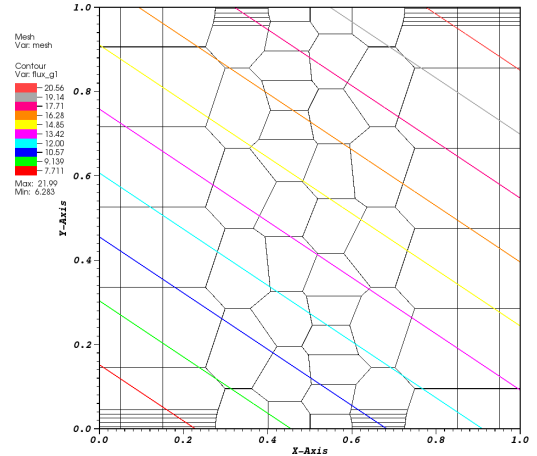
(c)



(d)



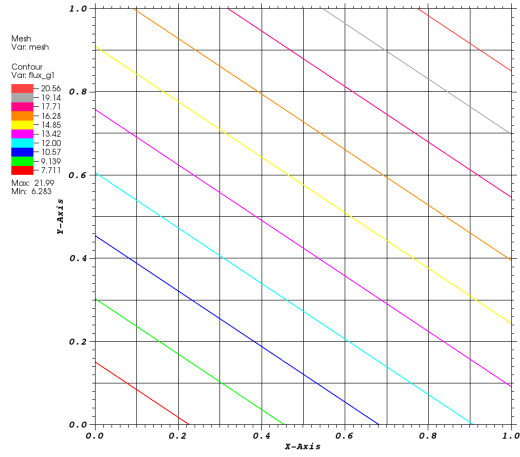
(e)



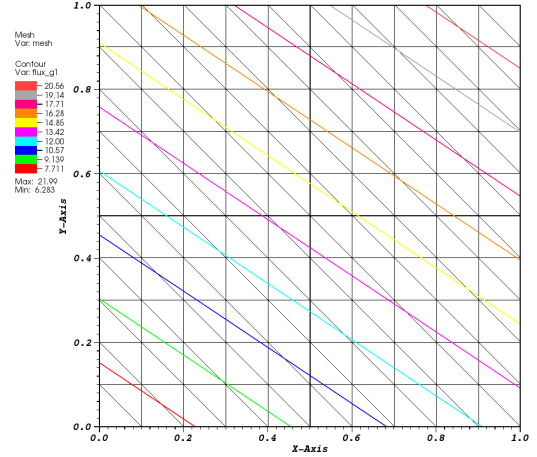
(f)

Figure 3.8: Contour plots of the exactly-linear solution with the PWL basis functions on (a) cartesian mesh, (b) ordered-triangular mesh, (c) quadrilateral shestakov mesh, (d) sinusoidal polygonal mesh, (e) quadrilateral z-mesh, and (f) polygonal z-mesh.

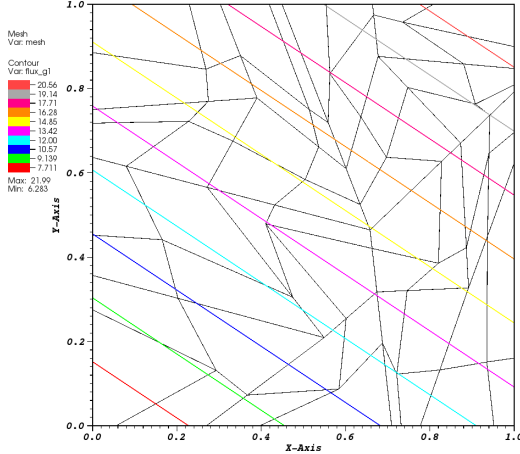




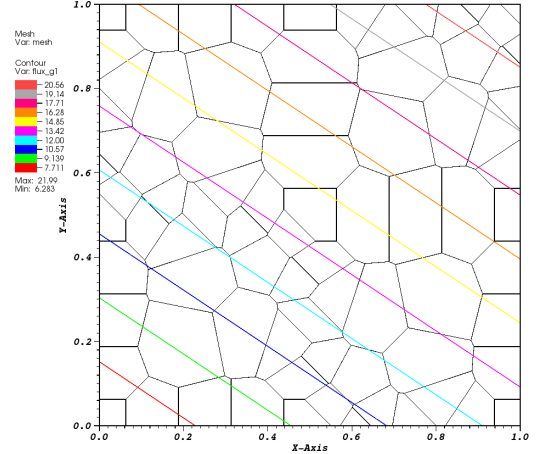
(a)



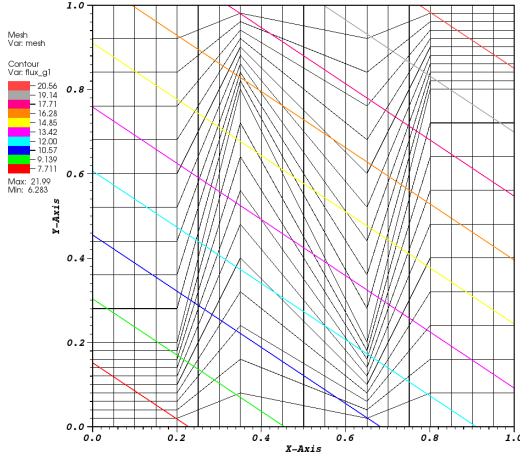
(b)



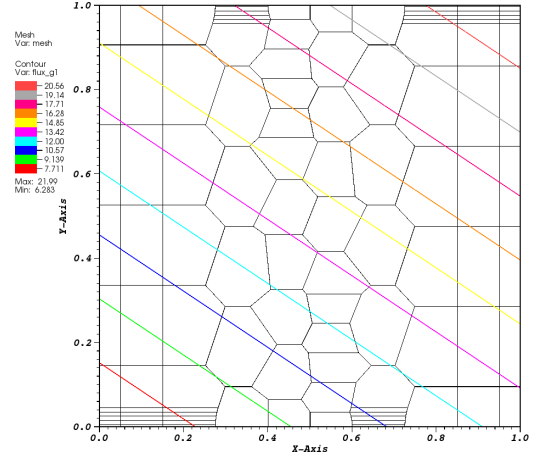
(c)



(d)

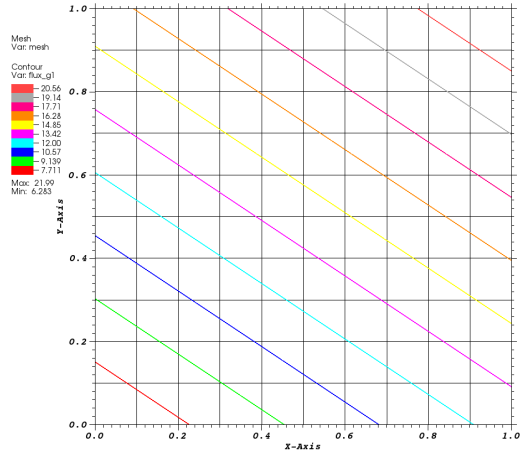


(e)

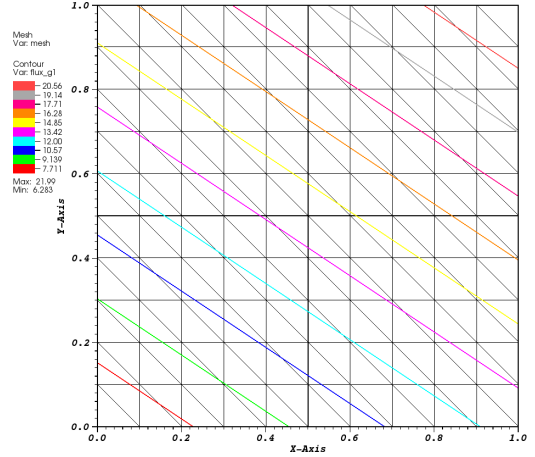


(f)

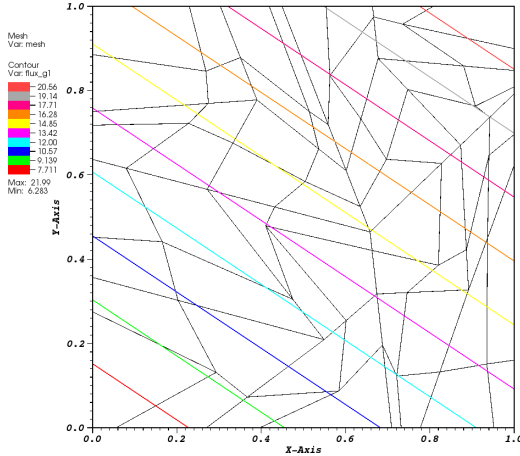
Figure 3.9: Contour plots of the exactly-linear solution with the mean value basis functions on (a) cartesian mesh, (b) ordered-triangular mesh, (c) quadrilateral shestakov mesh, (d) sinusoidal polygonal mesh, (e) quadrilateral z-mesh, and (f) polygonal z-mesh.



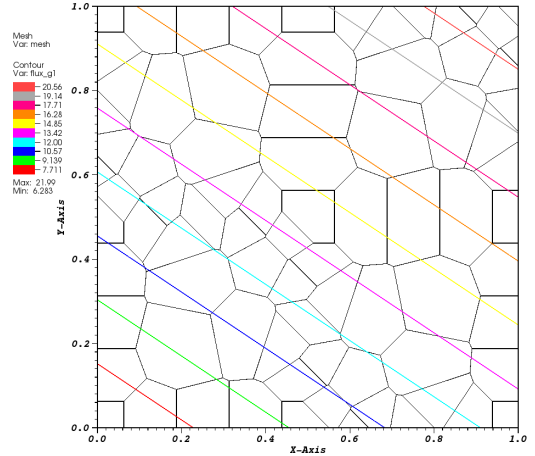
(a)



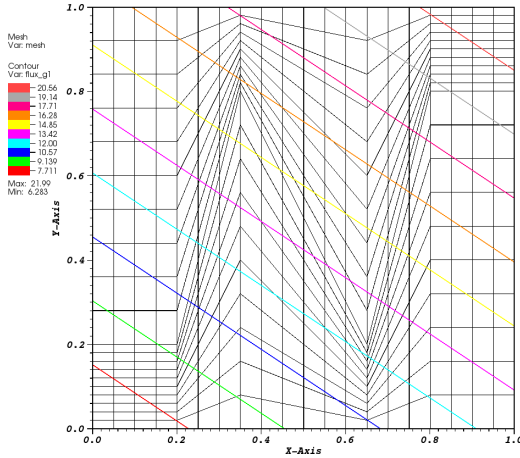
(b)



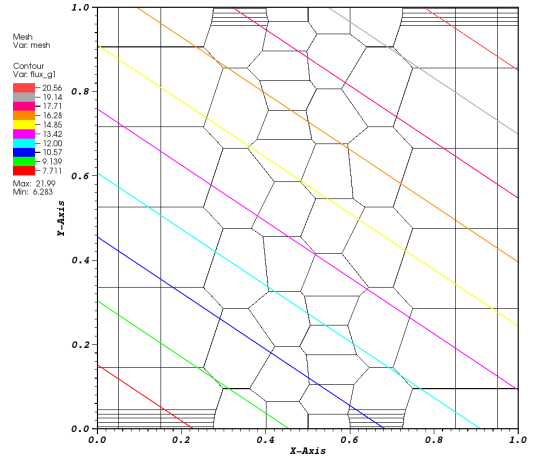
(c)



(d)

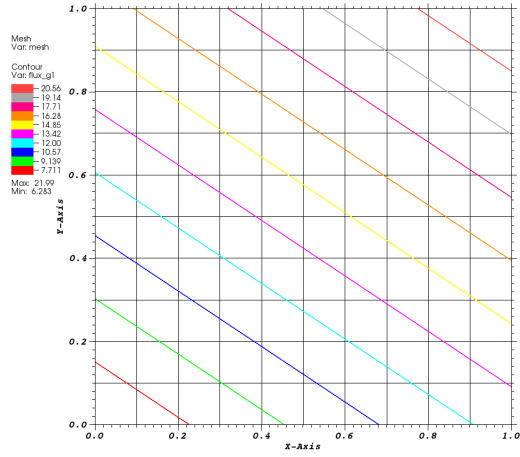


(e)

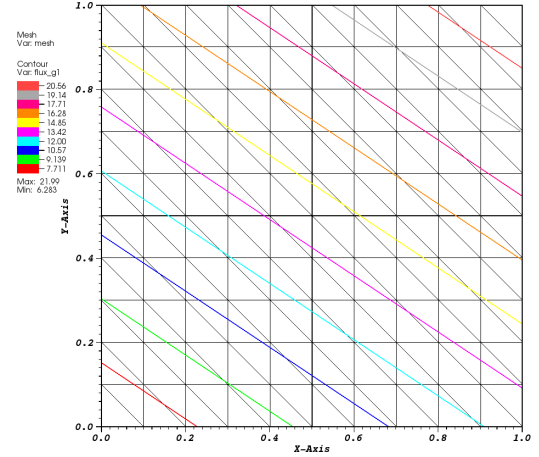


(f)

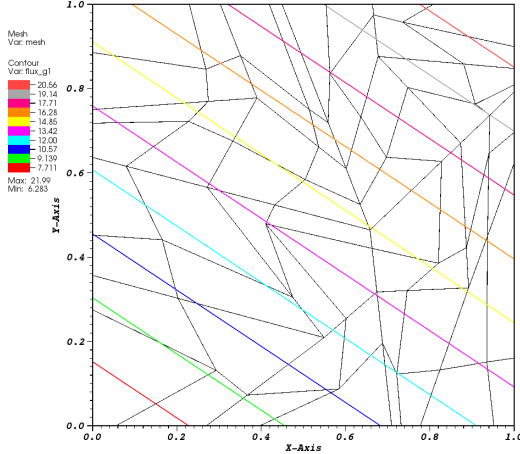
Figure 3.10: Contour plots of the exactly-linear solution with the linear maximum entropy basis functions on (a) cartesian mesh, (b) ordered-triangular mesh, (c) quadrilateral shestakov mesh, (d) sinusoidal polygonal mesh, (e) quadrilateral z-mesh, and (f) polygonal z-mesh.



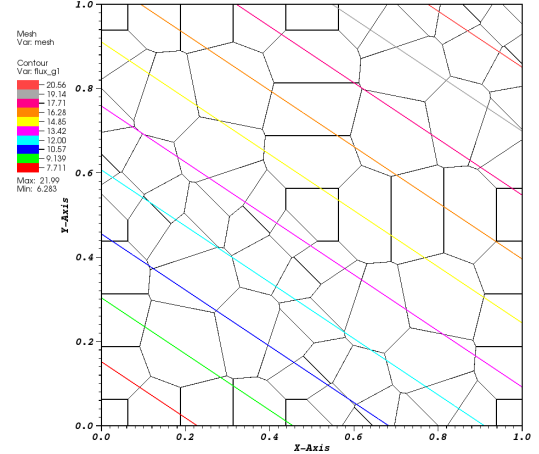
(a)



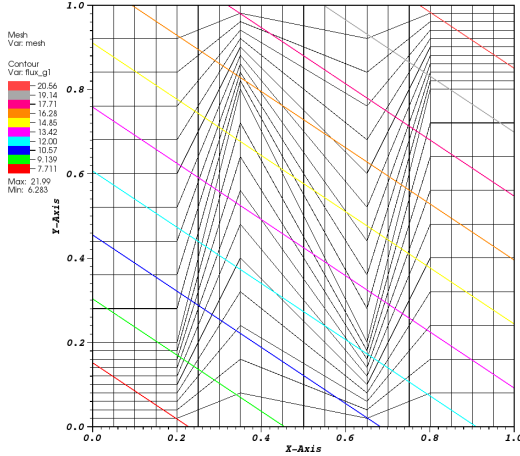
(b)



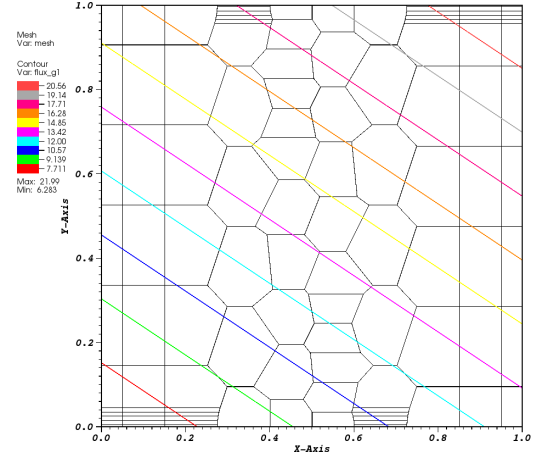
(c)



(d)



(e)



(f)

Figure 3.11: Contour plots of the exactly-linear solution with the quadratic serendipity maximum entropy basis functions on (a) cartesian mesh, (b) ordered-triangular mesh, (c) quadrilateral shestakov mesh, (d) sinusoidal polygonal mesh, (e) quadrilateral z-mesh, and (f) polygonal z-mesh.

driving source of the problem ( $Q_{ext}$ ). However, unlike MES, we enforce a spatial solution that cannot be captured by the interpolation of the finite element space. Using a specification of the Bramble-Hilbert [15] lemma, the difference between the exact solution,  $\Phi_e$ , and the discretized solution,  $\Phi_h$ , residing in the Sobolev space,  $W_D^h \in \mathcal{T}_h$ , for a given polynomial interpolation order,  $k$ , is

$$\|\Phi_e - \Phi_h\|_2 \leq C \frac{h^{q+1/2}}{(k+1)^q}, \quad (3.18)$$

where  $q = \min(k + 1/2, r)$ ,  $h$  is the maximum diameter of all mesh cells,  $C$  is some constant independent of the mesh,  $r$  is a measure of the regularity of the transport solution, and  $\|\cdot\|_2$  is the  $L_2$  norm [16]. For transport solutions with sufficient discontinuities,  $r$  can approach 0. However, if the chosen solution is at least  $C^k$  continuous and a topologically regular mesh is used, then the convergence rate becomes strictly  $(k+1)$ . For structured meshes,  $h$  is straightforward to define. Unfortunately, this becomes a problem in general for polytope meshes. Instead, the grid resolution can be related to the number of spatial degrees of freedom ( $N_{dof}$ ),

$$N_{dof} \propto h^{-d}, \quad (3.19)$$

where  $d$  is the dimensionality of the problem. Using this relationship for the grid resolution, along with the error norm of Eq. (3.18), we can define a general relationship between the error norm and the number of spatial degrees of freedom:

$$\|\Phi_e - \Phi_h\|_2 \propto N_{dof}^{-\frac{k+1}{d}}. \quad (3.20)$$

The result of Eq. (3.20) states that we expect convergence rates of  $N_{dof}^{-1}$  and  $N_{dof}^{-2/3}$  for linear basis functions in 2D and 3D, respectively. Conversely, quadratic basis

functions will yield convergence rates of  $N_{dof}^{-3/2}$  and  $N_{dof}^{-1}$  in 2D and 3D, respectively.

For this example, we choose the following solution and problem parameters and characteristics:

1. Constant total cross section so that parameterized material properties are not necessary;
2. No scattering to avoid solution discontinuities from the  $S_N$  discretization;
3. No solution dependence in angle to avoid introducing angular discretization error;
4. Analytical solutions that are  $C^\infty$  continuous in space for both the angular flux and 0th order flux moment - this leads to integrable solution spaces that satisfy the Bramble-Hilbert lemma no matter what polynomial order is selected for the basis functions;
5. The angular flux solution is zero on the boundary for all incident directions - this is identical to vacuum boundaries which can ease code development.

To satisfy these characteristics, we choose to analyze two different solution spaces. The first is a smoothly varying sinusoid solution with no extreme local maxima. The second solution is a product of a quadratic function and a gaussian which yields a significant local maximum.

The sinusoid flux solutions,  $\{\Psi^s, \Phi^s\}$ , have the following parameterized form,

$$\begin{aligned}\Psi^s(x, y) &= \sin\left(\nu \frac{\pi x}{L_x}\right) \sin\left(\nu \frac{\pi y}{L_y}\right), \\ \Phi^s(x, y) &= 2\pi \sin\left(\nu \frac{\pi x}{L_x}\right) \sin\left(\nu \frac{\pi y}{L_y}\right),\end{aligned}\tag{3.21}$$

where  $\nu$  is a frequency parameter. We restrict this parameter to positive integers ( $\nu = 1, 2, 3, \dots$ ) to maintain characteristic 5 of the solution and problem space. The gaussian solution space,  $\{\Psi^g, \Phi^g\}$ , that has its local maximum centered at  $(x_0, y_0)$  has the parameterized form,

$$\begin{aligned}\Psi^g(x, y) &= C_M x(L_x - x)y(L_y - y) \exp\left(-\frac{(x - x_0)^2 + (y - y_0)^2}{\gamma}\right), \\ \Phi^g(x, y) &= 2\pi C_M x(L_x - x)y(L_y - y) \exp\left(-\frac{(x - x_0)^2 + (y - y_0)^2}{\gamma}\right),\end{aligned}\tag{3.22}$$

where the constants in the equations are:

$$C_M = \frac{100}{L_x^2 L_y^2} \quad \gamma = \frac{L_x L_y}{100}.\tag{3.23}$$

For this example, we choose the dimensionality of our problem to be  $[0, 1]^2$  which makes  $L_x = L_y = 1$  for both the sinusoid and gaussian solutions. For the sinusoid solution, we select the frequency parameter,  $\nu$ , to be 3 and for the gaussian solution we set the local maximum:  $x_0 = y_0 = 0.75$ . With these parameters, the sinusoid solution will have local minima and maxima of  $-2\pi$  and  $2\pi$ , respectively, and the gaussian solution will have a global maximum of  $\frac{225}{32}\pi \approx 22.1$ .

### 3.4.3 Searchlight Problem

The next example models a beam or searchlight. Similar problems were investigated in Dedner and Vollmöller [17] and Wang and Ragusa [18]. In this problem, an incident beam of neutrons is shined onto a small portion of a boundary, propagates through a vacuum, and then exits through a small portion of a different boundary. As the beam propagates through the vacuum, the spatial discretization causes radiation outflow through all downwind cell faces. This leads to numerical dispersion

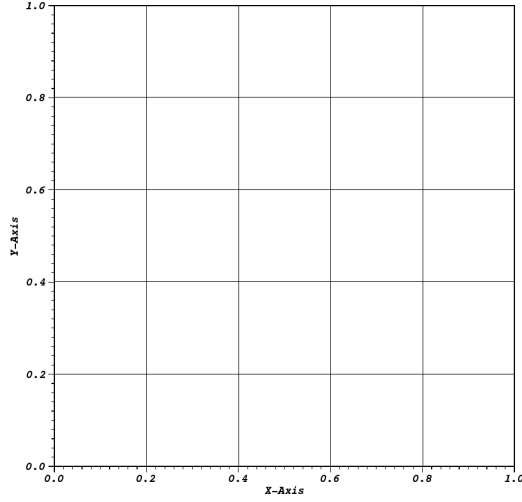


Figure 3.12: Initial mesh configuration for the searchlight problem before any refinement cycles.

and will cause the beam to artificially broaden.

In this problem, we investigate an  $\mathbb{R}^2$  domain of size  $[0, 1]^2$  cm. The radiation enters the left boundary between  $0.2 \leq y \leq 0.4$  with an un-normalized angular direction of  $[1, 0.4]$ . For this chosen direction, the radiation beam would analytically leave the right boundary between  $0.6 \leq y \leq 0.8$ . This means that any radiation leaving the right boundary for all other  $y$  values is due to the numerical dispersion of the beam.

We investigated this problem using several of the 2D polygonal basis functions as outlined in Sections 3.1 and 3.2 as well as

### 3.5 Conclusions

In this chapter, we have presented

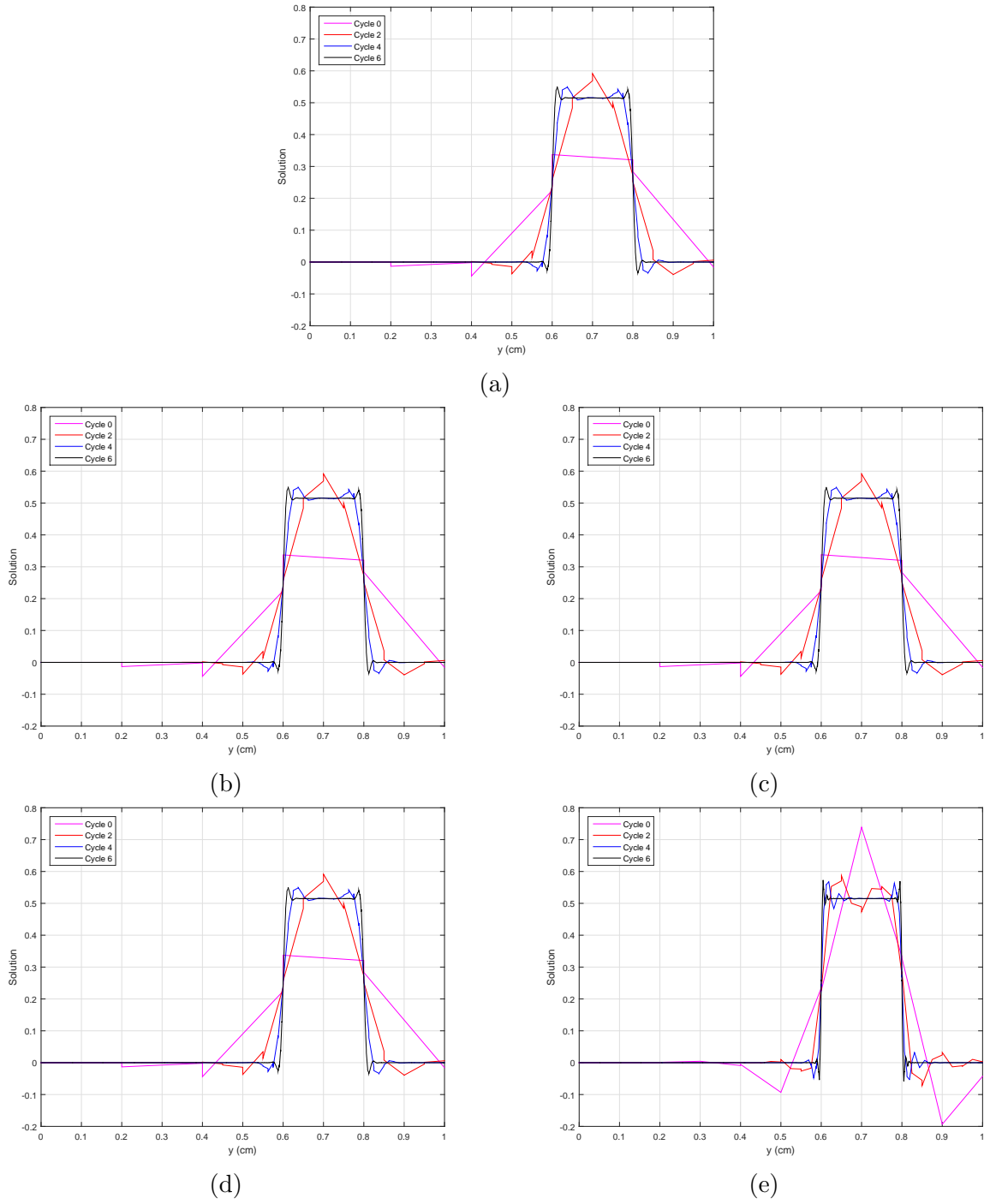


Figure 3.13: Exiting angular flux on the right boundary with uniform refinement using the (a) Wachspress basis functions, (b) PWL basis functions, (c) mean value basis functions, (d) linear maximum entropy coordinates and (e) quadratic serendipity maximum entropy coordinates.



## REFERENCES

- [1] R. LERNER and G. TRIGG, *Encyclopaedia of Physics*, 2 ed. (1991).
- [2] C. PARKER, *McGraw Hill Encyclopaedia of Physics*, 2 ed. (1994).
- [3] J. J. DUDERSTADT and W. R. MARTIN, *Transport theory*, John Wiley & Sons (1979).
- [4] K. OTT and W. BEZELLA, *Introductory Nuclear Reactor Statics*, American Nuclear Society (1989).
- [5] J. J. DUDERSTADT and L. J. HAMILTON, *Nuclear reactor analysis*, Wiley (1976).
- [6] E. E. LEWIS and W. F. MILLER, *Computational methods of neutron transport*, John Wiley and Sons, Inc., New York, NY (1984).
- [7] A. ERN and J.-L. GUERMOND, *Theory and practice of finite elements*, vol. 159, Springer Science & Business Media (2013).
- [8] T. A. WAREING, J. M. MCGHEE, J. E. MOREL, and S. D. PAUTZ, “Discontinuous finite element  $S_N$  methods on three-dimensional unstructured grids,” *Nuclear science and engineering*, **138**, 3, 256–268 (2001).
- [9] O. ZEINKIEWICZ, R. TAYLOR, and J. ZHU, *The finite element method: its basis and fundamentals*, Elsevier Butterworth-Heinemann (2005).
- [10] J. AKIN, *Application and implementation of finite element methods*, Academic Press, Inc. (1982).

- [11] T. S. BAILEY, *The piecewise linear discontinuous finite element method applied to the RZ and XYZ transport equations*, Ph.D. thesis, Texas A&M University (2008).
- [12] A. SHESTAKOV, J. HARTE, and D. KERSHAW, “Solution of the diffusion equation by finite elements in lagrangian hydrodynamic codes,” *Journal of Computational Physics*, **76**, 2, 385–413 (1988).
- [13] A. SHESTAKOV, D. KERSHAW, and G. ZIMMERMAN, “Test problems in radiative transfer calculations,” *Nuclear science and engineering*, **105**, 1, 88–104 (1990).
- [14] D. S. KERSHAW, “Differencing of the diffusion equation in Lagrangian hydrodynamic codes,” *Journal of Computational Physics*, **39**, 2, 375–395 (1981).
- [15] J. H. BRAMBLE and S. HILBERT, “Estimation of linear functionals on Sobolev spaces with application to Fourier transforms and spline interpolation,” *SIAM Journal on Numerical Analysis*, **7**, 1, 112–124 (1970).
- [16] P. HOUSTON, C. SCHWAB, and E. SÜLI, “Stabilized hp-finite element methods for first-order hyperbolic problems,” *SIAM Journal on Numerical Analysis*, **37**, 5, 1618–1643 (2000).
- [17] A. DEDNER and P. VOLLMÖLLER, “An adaptive higher order method for solving the radiation transport equation on unstructured grids,” *Journal of Computational Physics*, **178**, 2, 263–289 (2002).
- [18] Y. WANG and J. C. RAGUSA, “Standard and goal-oriented adaptive mesh refinement applied to radiation transport on 2D unstructured triangular meshes,” *Journal of Computational Physics*, **230**, 3, 763–788 (2011).